THE ASTROPHYSICAL JOURNAL, 464:738–759, 1996 June 20

NGC 3628: THE NUCLEAR MOLECULAR DISK AND EXPANDING MOLECULAR SHELLS

JUDITH A. IRWIN
Department of Physics, Queen's University, Kingston K7L 3N6, Canada; irwin@astro.queensu.ca
AND
YOSHIAKI SOFUE
Institute of Astronomy, The University of Tokyo, Mitaka, Tokyo 181, Japan; sofue@sof.mtk.ioa.s.u-tokyo.ac.jp
Received 1995 October 5; accepted 1996 January 8

ABSTRACT

CO emission from the nucleus of the edge-on starburst galaxy, NGC 3628 has been observed with the Nobeyama Millimeter-Wave Array at 125 pc resolution. Three main components are observed: a strongly centrally concentrated nuclear molecular disk with a steep velocity gradient, an offset low velocity gradient ridge, and numerous features indicative of expansion. The nuclear molecular disk, which dominates the emission, is centered at the nucleus of the galaxy which corresponds to the radio continuum peak. The CO spectra in the nuclear disk have been reproduced with an exponentially declining density distribution of radial scale length of 228 pc, a vertical scale height of 49 pc, and a velocity dispersion of 36–45 km s^{-1}. Energy input from embedded star-forming activity can account for the observed velocity dispersion. Four expanding shells have been identified with kinetic energies of order 10^{52}–10^{54} ergs, mostly associated with the low velocity gradient ridge outside of the nuclear disk. The shells appear to have arisen in a single starburst which has occurred within the last few $\times 10^6$ yr. CO extensions are observed out to 430 pc from the plane as well as a CO velocity cone opening away from the disk toward the north, suggesting that molecular disk-halo outflow is occurring. The most obvious outflow feature is situated $\approx 20''$ to the west of the nucleus, which corresponds to the apparent origin of the kiloparsec-scale southern Hα plume.

Subject headings: galaxies: individual (NGC 3628) — galaxies: ISM — galaxies: kinematics and dynamics — galaxies: nuclei — galaxies: starburst — radio lines: galaxies

1. INTRODUCTION

NGC 3628 is one of a growing number of spiral galaxies displaying bipolar outflow from the nuclear region. In this category, probably the most well-defined example is the nuclear radio lobe galaxy, NGC 3079 (Seaquist, Davis, & Bignell 1978), which appears to be driven by a compact nuclear radio source (Irwin & Seaquist 1988). However, unlike NGC 3079, the nuclear bipolar outflow of NGC 3628 likely originates from a starburst (Condon et al. 1982) and rather than a well-defined lobe, the radio continuum emission along the minor axis resembles a "spur" extending far from the plane of this edge-on galaxy. This radio spur as well as a spectral "break" observed in the integrated radio emission were the first indications that NGC 3628 could be experiencing a galactic wind (Schlickeiser, Werner, & Wielebinski 1984). The outflow was later confirmed by Fabbiano, Heckman, & Keel (1990), who observed a spectacular X-ray plume extending ≈ 12 kpc along the minor axis as well as extraplanar kiloparsec-scale Hα plumes. In this respect, NGC 3628 closely resembles the well-known starburst galaxies, NGC 253 and M82 (Fabbiano 1988), both of which display X-ray emission out to ≈ 9–10 kpc among the minor axis.

NGC 3628 is a member of the interacting Leo Triplet (=Arp 317), which includes NGC 3627 and NGC 3623. A fourth galaxy, NGC 3593, is also a member of the group (Garcia 1993) The interaction has been modeled by Rots (1978) and is believed to be responsible for asymmetries in the H I distribution of NGC 3628, an H I plume extending more than 90 kpc toward the east, and an intergalactic H I bridge toward the south (see also Haynes, Giovanelli, & Roberts 1979; Wilding, Alexander, & Green 1993), dramatically illustrated in Haynes, Giovanelli, & Chincarini (1984). The distance to the Leo group is variously quoted from 6.7 to 23.4 Mpc. We will adopt the lower value for consistency with earlier CO work and also to minimize masses and energy-related quantities. The distance dependence of derived quantities will be shown through the scaling factor, $\mathcal{D}$, which is the distance in units of 6.7 Mpc.

NGC 3628, itself, is of type Sb (peculiarities, spindle) in de Vaucouleurs's classification system (de Vaucouleurs et al. 1991, hereafter RC3) and has been well studied in various wave bands. Far-IR observations suggest a dust temperature of 45 K and a total luminosity of $L_{\rm FIR} = 10^{10.5}\ L_\odot$ (Rickard & Harvey 1984; Rice et al. 1988), and a conspicuous dust lane is present in optical images (e.g., Wray 1988). Radio continuum maps show extended disk emission with an embedded strong compact nuclear source $\approx 160 \times 35$ pc in size (van der Hulst, Crane, & Keel 1981; Condon et al. 1982; Condon 1987; Condon et al. 1990), which resolves into many smaller parsec-scale components (Carral, Turner, & Ho 1990). The polarization vectors at 2.8 cm are roughly parallel to the plane (Dumke et al. 1995). Absorption lines of H I, OH, and H_2CO have been detected against this nuclear continuum source (Rickard, Bania, & Turner 1982; Schmelz, Baan, & Haschik 1987a, b; Baan & Goss 1992) and suggest the presence of an inner rotating neutral disk as well as another "anomalous" blueshifted feature with a lower velocity gradient; Baan & Goss suggest that the latter feature results from the tidal interaction. HCN emission peaking at the radio continuum core has also been reported recently (L. Blitz, private communication). Anantharamaiah

et al. (1993) have shown that H92α recombination line emission in the nuclear region is consistent with an origin from 280 H II regions ≈1 pc in size.

Previous CO studies have consisted of single-dish observations by Rickard, Turner, & Palmer (1985), Young, Tacconi, & Scoville (1983), Boisse, Casoli, & Combes (1987), Israel, Baas, & Maloney (1990), Reuter et al. (1991), and Braine et al. (1993) at spatial resolutions ranging from 12″ to 65″. The molecular gas is strongly centrally concentrated, with enhancements along the disk which may represent spiral arms and/or molecular rings superimposed on a diffuse background of CO emission. The presence of a dense, rapidly rotating central molecular disk of order ≤6″ (≤200 pc) rotating at ≥150 km s^{-1} is suggested from these studies, but this disk had heretofore remained spatially unresolved. It was with this purpose that we undertook interferometric CO observations of NGC 3628 with the Nobeyama Millimeter-Wave Array (NMA). At a distance of 6.7 Mpc, the NMA spatial resolution of 3.″85 corresponds to 125 pc, or roughly the size of a giant molecular cloud complex in the Milky Way. The relative proximity of NGC 3628 as well as its edge-on orientation ($i = 89°$) make this galaxy an ideal candidate for detailed study of the inner molecular disk and its relationship to the nuclear outflow.

2. OBSERVATIONS AND DATA REDUCTION

The ^{12}CO(1–0) observations of NGC 3628 were made using the NMA in the C and D (compact) configurations. The D-array observations were made on 1993 January 12 and February 4, and the C-array observations were made on 1993 March 9 and 17. The synthesized main beam had a FWHM of 3.″93 × 3.″79 (128 × 123 pc) at a position angle of 33.°14. The field center was placed at the kinematic center of the ^{12}CO(2–1) emission found by Reuter et al. (1991) using the Institut de Radioastronomie Millimétrique (IRAM) telescope, i.e., R.A. = 11^{h}17^{m}39.^{s}30 and decl. = 13°51′47.″0 (epoch 1950). This agrees with the optical center (R.A. = 11^{h}17^{m}39.^{s}6, decl. = 13°51′48″; Dressel & Condon 1976) to within the quoted errors. The phase and bandpass calibrations were made using the radio sources 1055+018 and 3C 273, respectively. The flux calibrator was 1055+018, which had a flux density of 2.5 Jy on March 14 and 2.8 Jy on March 22 at 114.95 GHz; we adopt the mean value of 2.65 Jy, which introduces an error of ≈5% into the intensity scale. The center frequency was set to 114.9561294 GHz, corresponding to the kinematic LSR recession velocity (radio definition) of 820 km s^{-1} = $V_{LSR} \approx V_\odot$ determined by Reuter et al. (1991) from the ^{12}CO(2–1) emission. This is blueshifted by ≈22 km s^{-1} from the 21 cm systemic velocity (843 km s^{-1}, Tifft & Cocke 1988; 841 km s^{-1}, Wilding et al. 1993). The data acquisition was made with SIS receivers equipped on the five antennae, and the data were processed with a FACOM VP200 vector processor. A 1024 channel FX system (a fast Fourier transform spectro-correlator) was used for the spectroscopic data acquisition with a total bandwidth of 320 MHz (831 km s^{-1}). The data were then averaged in 16 bins of original frequency channels resulting in 64 channels with a frequency (velocity) resolution of 5 MHz (13.0 km s^{-1}). We used the central 41 binned channels spanning 200 MHz or 520 km s^{-1}. These data were Fourier transformed to the image plane and then CLEANed using the Astronomical Image Processing System (AIPS). The rms noise in the final channel maps was ≈65 mJy beam^{-1}. For quantitative calculations and modeling, we then corrected for the primary beam, which had a FWHM of 60″. Displayed images, however, are shown without the primary beam correction (unless otherwise stated). Since the shortest baseline is 20 m, the largest angular size visible is of order 25″.

3. RESULTS

The cleaned maps have been combined into a cube of intensity data in (R.A., decl. V_{LSR}) space and also transposed to (V_{LSR}, X, Y) space, where X and Y are coordinates parallel and perpendicular to the major axis of the galaxy at P.A. = 107° and 17°, respectively. Using these cubes, we have obtained various diagrams and spectral information, which we describe below.

3.1. *Spectra*

Figures 1*a*–1*b* show the spectra at 6″ and 3″ grid intervals, respectively, aligned with the galactic plane. The spectra are complex, showing wide, double, and/or multiple peaks. It is evident that the molecular gas distribution is asymmetric about the field center (0, 0 = 11^{h}17^{m}39.^{s}30, 13°51′47.″0) with most of the emission lying to the east of this position. We will argue in § 3.4 that the galaxy nucleus is actually ≈15″ to the east of our field center, near the high-resolution (0.″2) 15 GHz radio continuum peak (Carral et al. 1990), i.e., near R.A. = 11^{h}17^{m}40.^{s}35, decl. = 13°51′46.″0. The strongest CO emission and widest spectra center at the nucleus, for example, the maximum intensity of 1.20 Jy beam^{-1}, occurs at R.A. = 11^{h}17^{m}40.^{s}46, decl. = 13°51′46.″2, V_{LSR} = 875.9 km s^{-1}. This maximum is equivalent to a Rayleigh Jeans brightness temperature of 7.5 K T_B using 6.21 K (Jy beam^{-1})$^{-1}$.

Figure 2 shows the global profile of the emission, which has a rough double-horned appearance, typical of a rotating inclined disk. The full width at 20% of maximum is 350 km s^{-1}, which reduces to 240 km s^{-1} at the 50% level. As Figures 1*a*–1*b* indicate, the large velocity width is due mainly to spectra taken in and near the galaxy center, suggesting a high velocity dispersion and/or high rotational velocity in the nucleus. The midpoint of this profile yields a systemic velocity of V_{LSR} = 841 ± 10 km s^{-1}. This velocity is redshifted by 21 km s^{-1} from our band center [set to the CO(J = 2–1) peak] but is in excellent agreement with previous H I measurements (843 km s^{-1}, Tifft & Cocke 1988; 841 km s^{-1}, Wilding et al. 1993). The integrated intensity of the global profile is 2.05 × 10^3 Jy km s^{-1}, corresponding to 12.7 × 10^3 K km s^{-1} over all detected emission. This will be a lower limit due to the insensitivity of the interferometer to broad spatial scales. A total H_2 mass can be determined from this value by assuming that the Galactic N_{H_2} (cm^{-2}) to $I_{CO} = \int T_R^* dV$ (K km s^{-1}) conversion factor is applicable to the nuclear region of NGC 3628. We adopt the factor 3 × 10^{20} cm^{-2} (K km s^{-1})$^{-1}$ (Young & Scoville 1991), where we take $T_R^* \approx T_B$ and introduce a scaling factor, $\mathscr{X}$, which is the conversion factor in units of 3 × 10^{20} cm^{-2} (K km s^{-1})$^{-1}$. Then a total H_2 mass of 7.4 × 10^8 $\mathscr{X}$ $\mathscr{D}^2$ $M_\odot$ is derived for the central ≈2.6 × 0.6 kpc (80″ × 20″) of this galaxy. For comparison, Boissé et al. (1987) find a value of 2.3 × 10^8 $M_\odot$ within a smaller 800 pc region from IRAM ^{12}CO(1–0) observations, and Reuter et al. (1991) find an H_2 mass of 1.4 × 10^9 $M_\odot$ within the larger central 4 kpc × 1 kpc from IRAM ^{12}CO(2–1) observations (adjusting both values to the same conversion factor).

The dependence of derived quantities on $\mathscr{X}$ will be shown

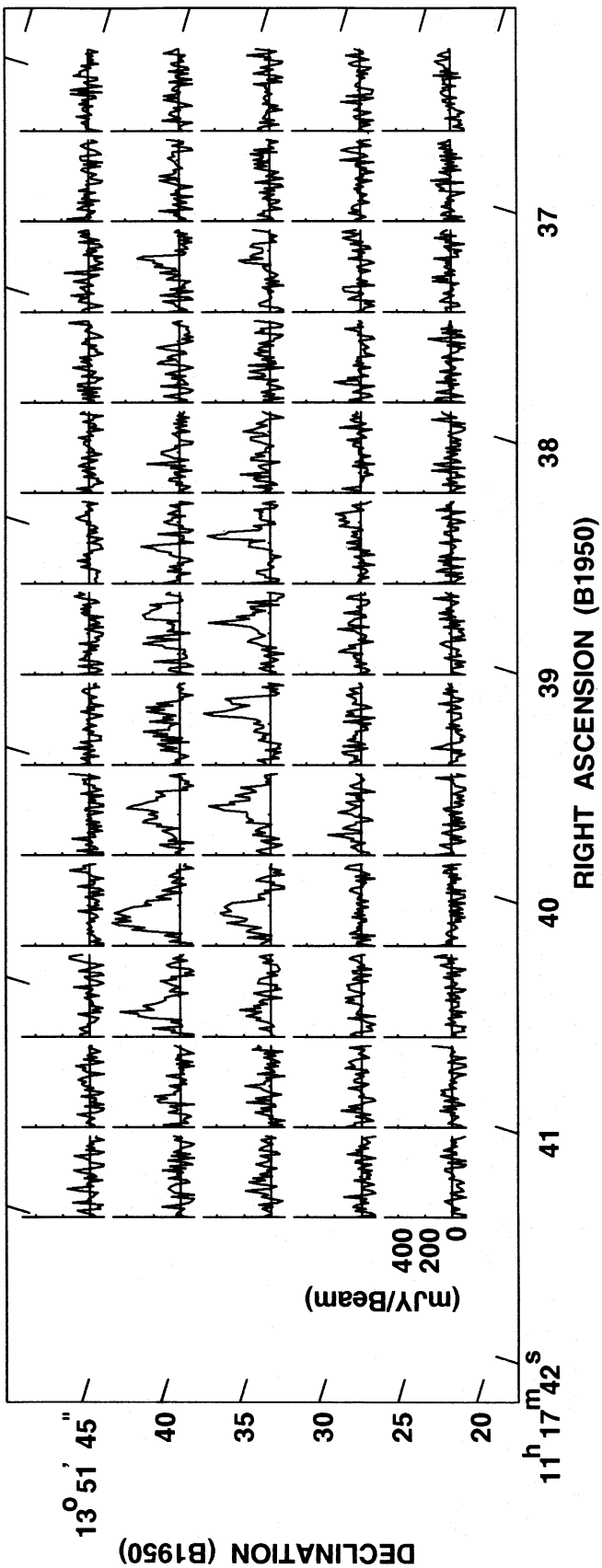

FIG. 1*a*

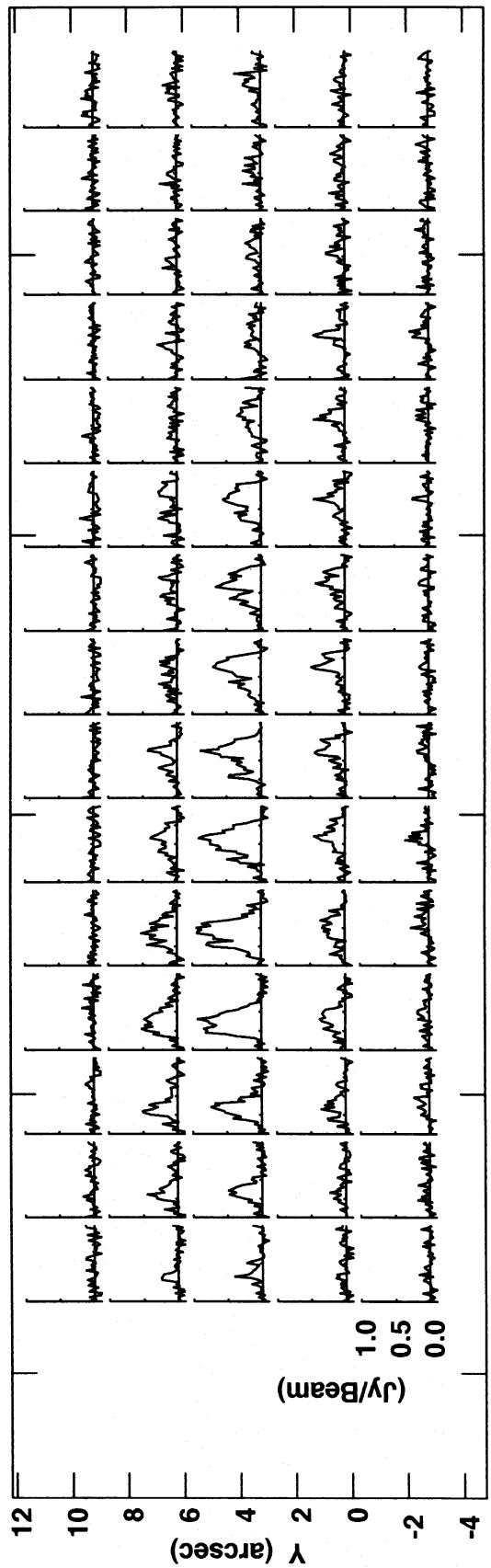

FIG. 1*b*

FIG. 1.—(*a*) CO line spectra shown at 6″ grid intervals, parallel and perpendicular to the galaxy's major axis. The *X*-axes in each small panel extend for 520 km s^{-1} from 1097 km s^{-1} (*left*) to 577 km s^{-1} (*right*). The *Y*-axes are shown from −0.1 to 0.5 Jy. (*b*) Same as (*a*), but showing a smaller region of the galaxy at 3″ grid intervals, and the *Y*-axes range from −0.1 to 1.0 Jy. The frame center (0, 0) is set at the field center (which is offset from the galaxy nucleus). (*c*) Same as (*b*), but showing model spectra from Table 1, col. (*2*). (*d*) Same as (*b*), but showing model spectra from Table 1, col. (*4*) (best fit overall).

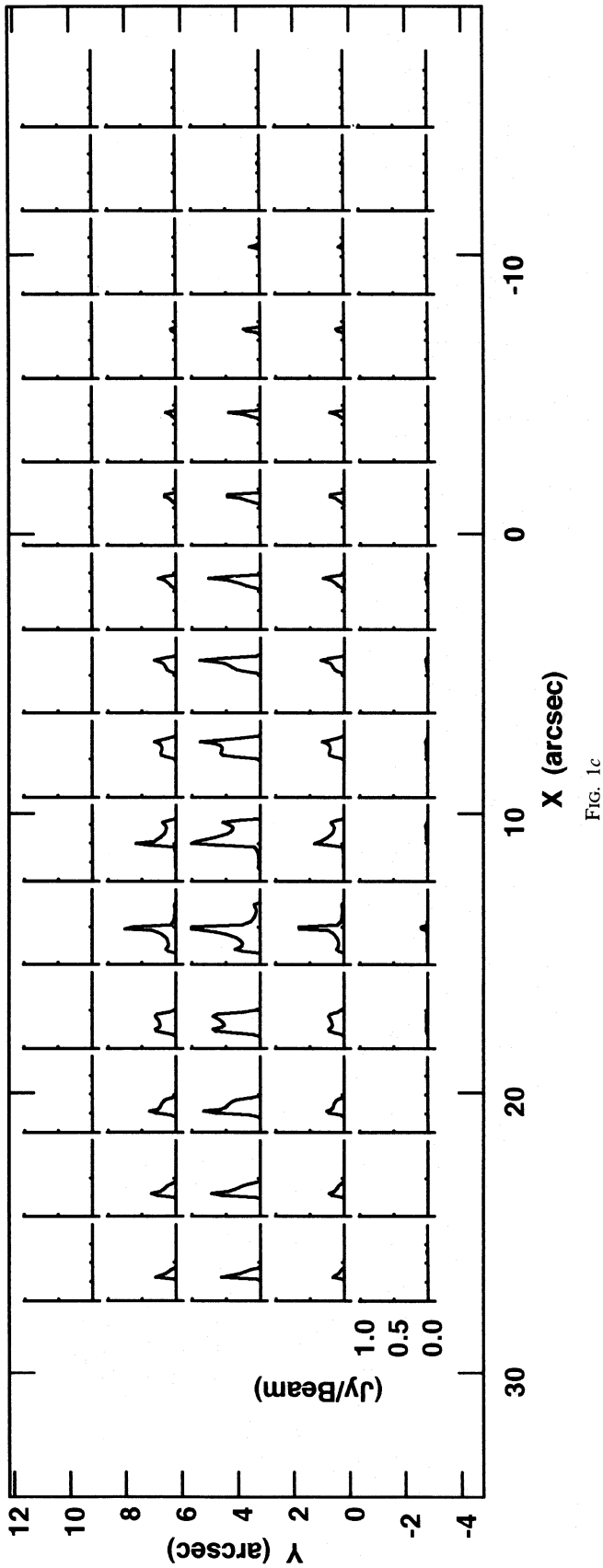

FIG. 1c

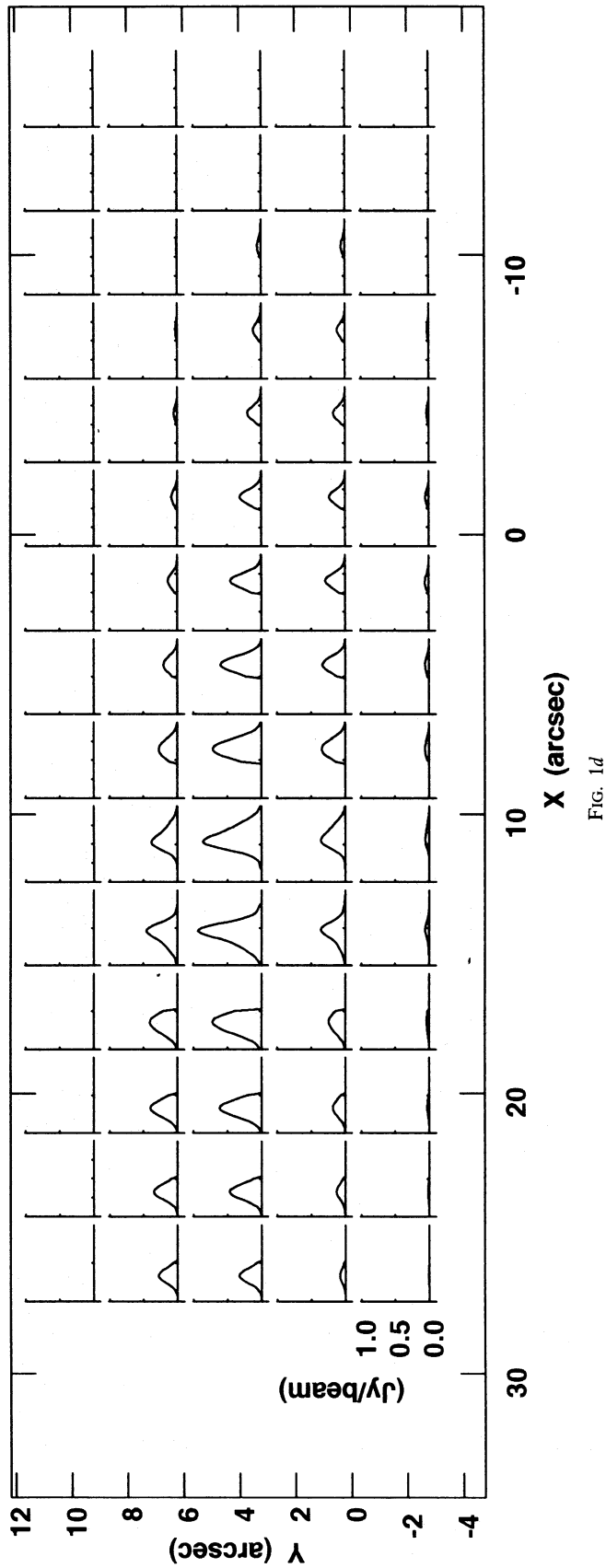

FIG. 1d

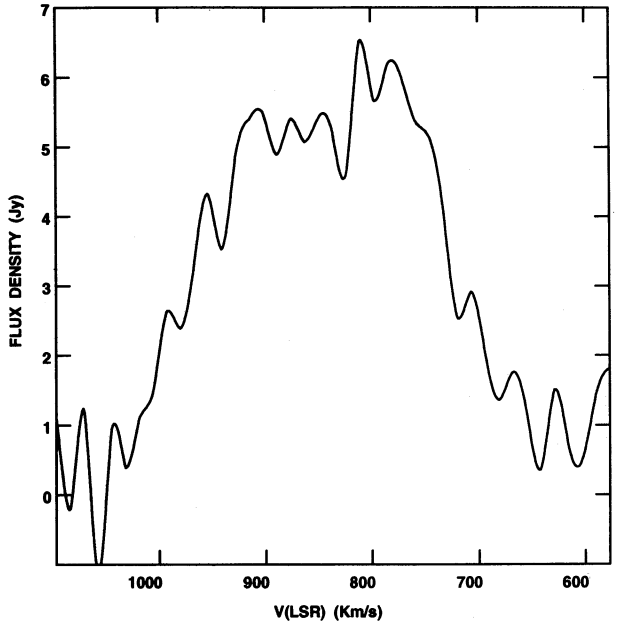

FIG. 2.—CO global profile of NGC 3628

throughout this paper, and the CO–H_2 conversion factor will be discussed more fully in § 3.5.

3.2. *Channel Maps*

Figure 3 shows unrotated channel maps at 13.0 km s^{-1} intervals. The concentration of gas near the radio continuum core/nucleus ($11^h17^m40^s.35$, 13°51′46″.0) rather than the field center ($11^h17^m39^s.30$, 13°51′47″.0) is evident, as well as an asymmetry such that more extended emission is seen to the west of the nucleus. It is clear that the northwest disk is advancing and the southeast disk is receding, consistent with large-scale galaxy rotation. From the orientation of the dust lane across NGC 3628, it is apparent that the southern edge of the galaxy is the nearer one to us. Therefore, any trailing spiral structure would appear to have an inverted **S** shape when projected onto the sky. No obvious inverted **S** signature is evident in the channel maps, though the galaxy's nearly edge-on orientation would tend to mask it, in any event.

Particularly interesting are a number of CO extensions and what appear to be partial arcs extending away from the plane, especially toward the south (see, e.g. $V = 966.90$, 849.93, 836.94, 810.94, 758.96, 706.97 km s^{-1}, and others). These will be discussed more fully in § 3.10.

3.3. *Total Intensity Map and Velocity Field*

Figure 4*a* is an unrotated total intensity map obtained by integrating the channel maps over all emission. The radio continuum peak (east) and IRAM CO(2–1) kinematic center (our field center, west) are marked with crosses. An intensity slice along the major axis of the distribution is shown in the inset. The CO emission is strongest at the radio continuum peak (the galaxy nucleus, see § 3.4) and then falls off rapidly. A fit to the main peak of the (primary beam corrected) slice results in a $1/e$ scale length of approximately 9″ (≈290 pc). The asymmetry is apparent, with more extended emission to the west than to the east of the nucleus, and there is also a secondary peak near the field center (see inset, $X = 0$). The half-intensity radius of the disk from the center is ≈7″ (227 pc) toward the east and ≈15″ (487 pc) to the west, indicating that the nuclear disk is compact. However, weak emission can be traced out to at least 50″ (1.6 kpc) along the galaxy plane to the west and 35″ (1.1 kpc) to the east of the nucleus. Throughout most of the emission region, the disk appears quite flat, but in the outermost regions there is a very weak inverted **S** curvature. The shape of the curvature is consistent with that expected from spiral structure. However, it is also in the same sense as the warp observed by Wilding et al. (1993) at large radii in the northwest H I disk which they attribute to tidal effects. The full extent of the flat part of the disk, excluding the curved outer regions, is ≈40″ (1.3 kpc). Faint CO extensions to the south of the plane are also obvious in this figure. These can be traced out to ≈13″ from the midplane, or ≈430 pc in projection.

Figure 4*b* shows the (unrotated) intensity weighted mean velocity field, (first moment map, van Gorkom & Ekers 1986). The velocity field is very distorted, especially on the western side. From the shape of the isovelocity contours, the systemic velocity clearly centers more closely on the radio continuum peak (eastern cross), rather than the CO(2–1) kinematical center (western cross), consistent with a nucleus at the radio continuum peak. If a region within only ±20″ of the nucleus is isolated, the velocity field appears much more regular, but the kinematic major axis curves strongly toward the south (both on the east and west sides) with increasing radii. A curving kinematic major axis is often interpreted as a warp in the disk, but this contrasts sharply with the very flat appearance of the emission over the same region in Figure 4*a*. As a test, we formed the first moment map again, excluding all lower level emission, and we have found that the curvature diminishes. Therefore, the apparent curvature in the kinematic major axis appears to be due to contributions from low-level emission at anomalous velocities, rather than a real warp in these inner regions (see also §§ 3.4 and 4.4).

There are some interesting peculiar velocities visible in Figure 4*b*. The most obvious forms an apparent cone about 20″ to the west of the nucleus whose apex is embedded in the disk and which opens northward. Velocities in the cone become increasingly redshifted with northward distance from the major axis. There is no obvious counterpart in the total intensity image of Figure 4*a*, but there are extensions in this vicinity to the south of the plane. We will show in § 3.10 that there is an expanding molecular shell at the apex of this cone. A few arcseconds to the west of the nucleus, the isovelocity contours also stretch out strikingly toward the northwest. This region also appears to form a northward opening cone, with some evidence for higher redshifts toward the north, though this region is not as well defined as the cone 20″ to the west of the nucleus. A southern extension, possibly associated with this feature, is also seen a few arcseconds west of the nucleus in Figure 4*a*.

3.4. *Position-Velocity Diagrams*

Figure 5 shows position-velocity diagrams parallel to the major axis, X, at several different heights from $Y = -10''$ to $Y = +5''$, and Figure 6 shows an averaged $X-V$ diagram for emission within $Y = \pm 5''$. The distribution in $X-V$ space is complex and asymmetric. There is clearly more weaker emission to the west of the nucleus and also toward the south of the major axis (negative numbered frames in Fig. 5), as previously illustrated in Figure 4*a*. The strongest emission, however, clearly occurs in a nuclear disk with a steep velocity gradient (Fig. 6). Five bright components

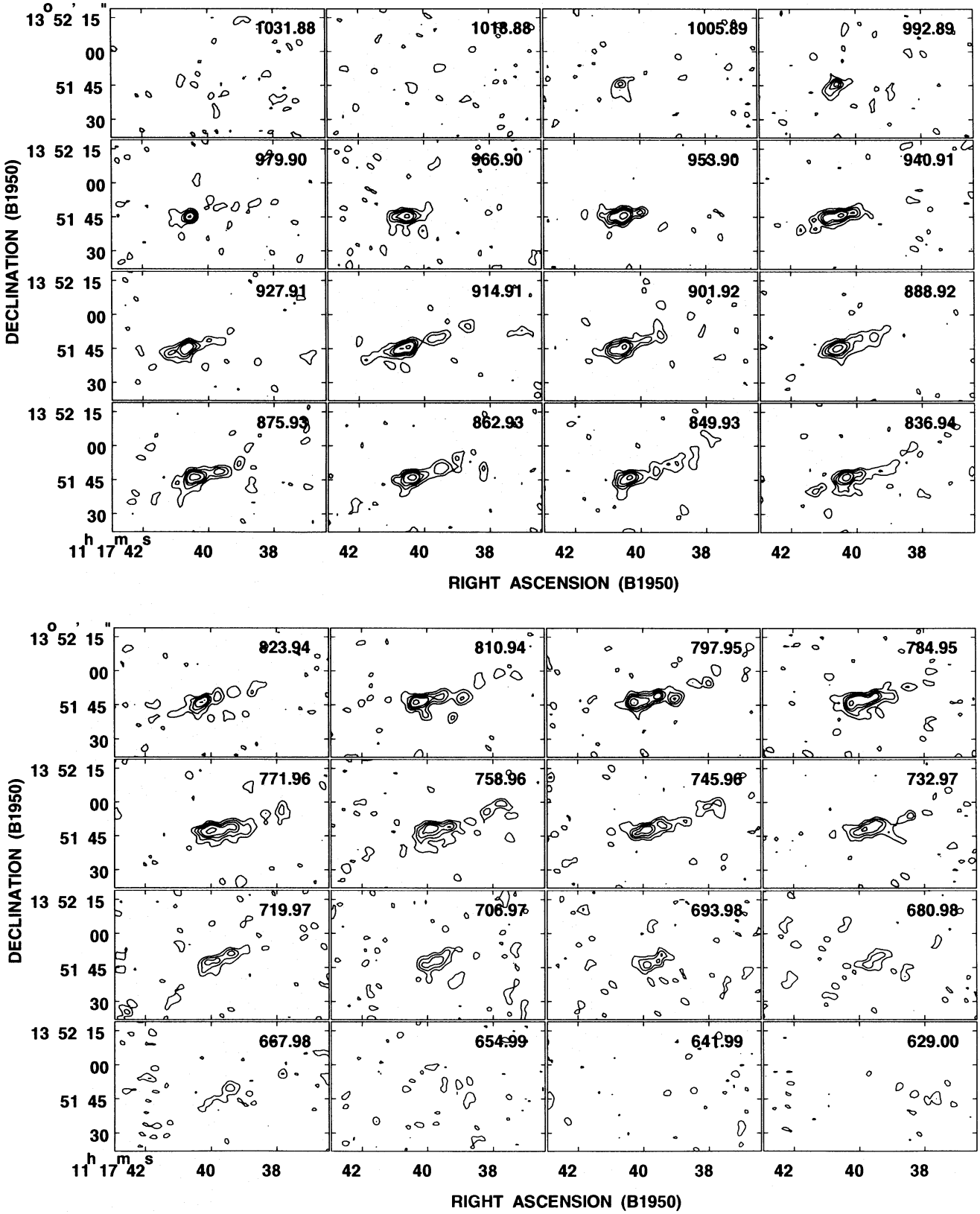

FIG. 3.—Channel maps of the CO line intensity (unrotated). V_{LSR} is indicated in each panel. Contours are at 0.1325 × 1 (≈2 σ), 2, 3, 4, 6, and 8 Jy beam^{-1}.

(some with substructure) delineate a ridge of strong emission with the central component situated at the midpoint of the ridge both in right ascension and in velocity. The central bright CO component corresponds in position to the radio continuum peak. The (0, 0) point in Figure 6 has been set to the radio continuum center and a velocity of 840 km s^{-1} (i.e., the midpoint of the global profile).

It is clear from Figure 6 that the galaxy nucleus cannot be ≈15″ to the west of the nucleus adopted here, i.e., it cannot be at the IRAM CO(J = 2–1) kinematic center = our field center. The optical center of the galaxy, which is closer to the CO(2–1) center, also cannot be reconciled with this distribution. The CO peak, the midpoint of the bright CO emission which delineates the nuclear molecular disk, and

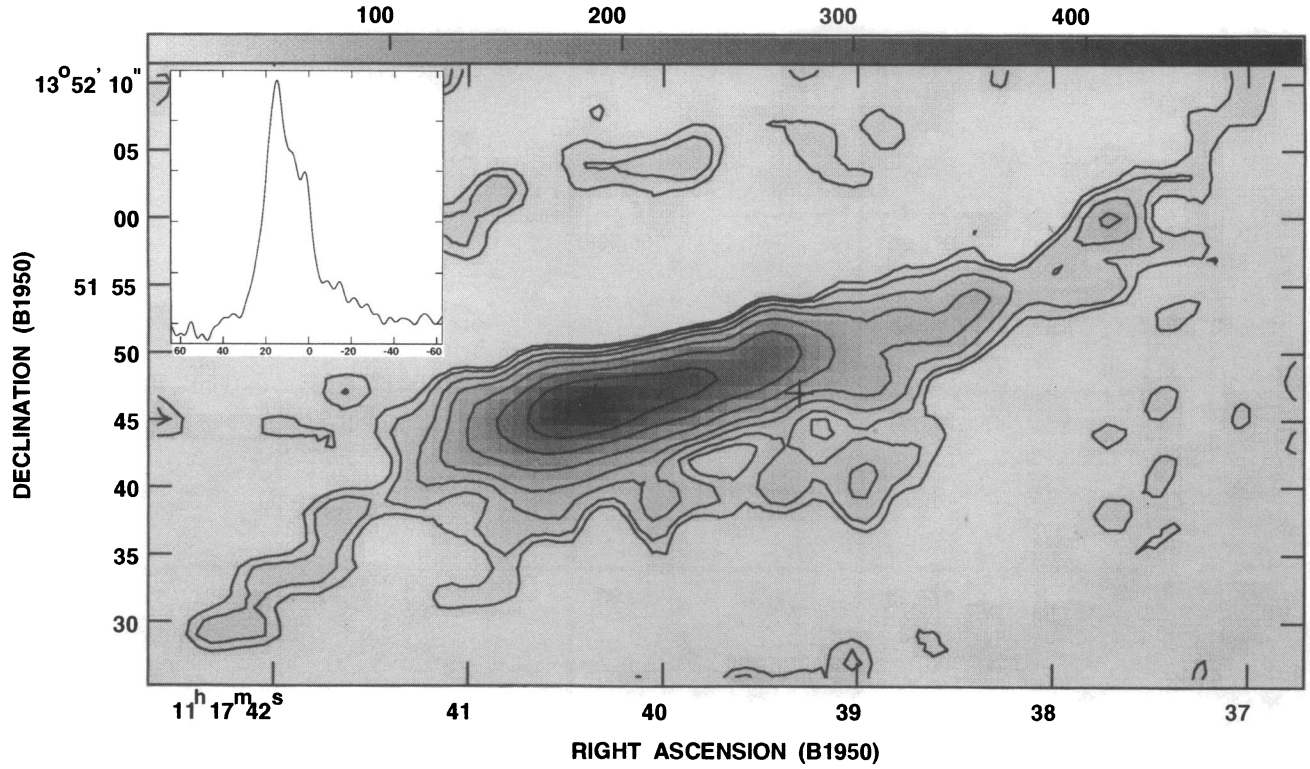

FIG. 4*a*

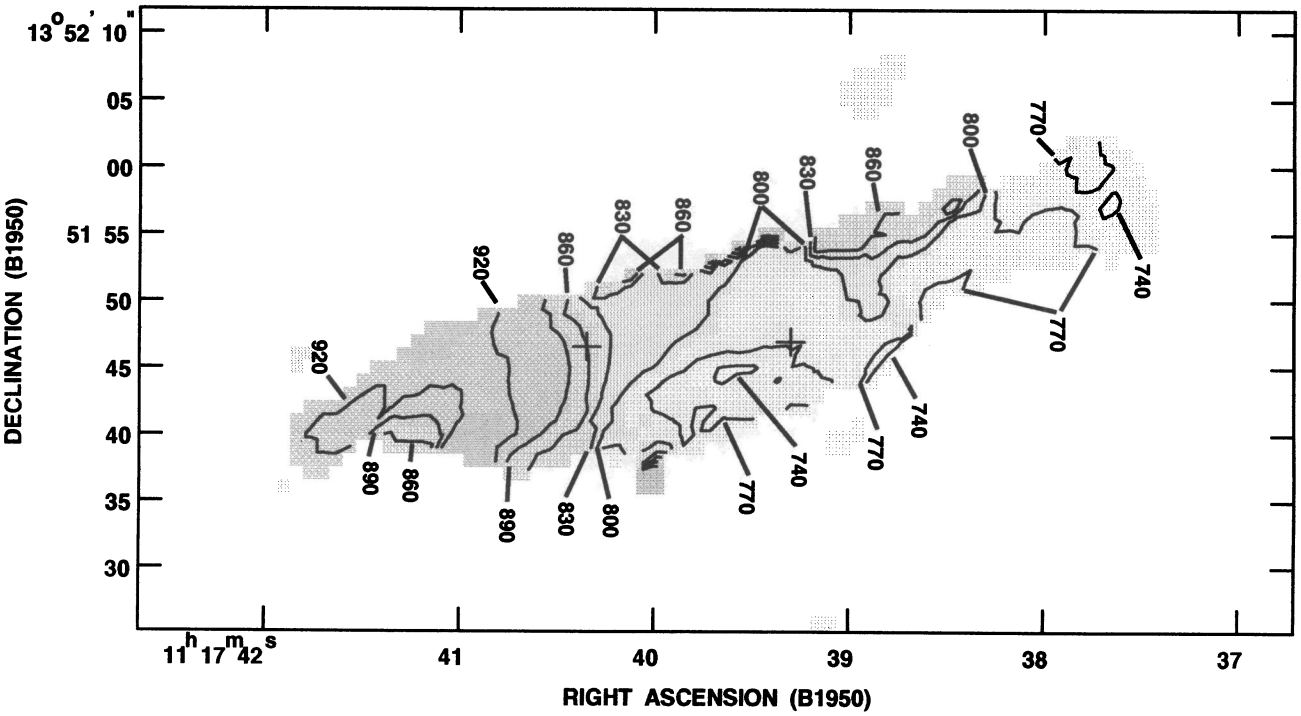

FIG. 4*b*

FIG. 4.—(*a*) Total intensity distribution, obtained by integrating over 28 channels from 655 km s^{-1} to 1006 km s^{-1}. Contours are at 0.364 × 20, 30, 50, 75, 125, 200, 300, and 450 Jy beam^{-1} km s^{-1}. A cross marks the field center (west) and radio continuum peak (east at position of strongest emission). The fainter emission running parallel to the major axis approximately 17″ to the north is due to constructive addition of low-level sidelobes. *Inset*: Intensity slice along the major axis. The *X*-axis shows offsets (arcseconds) from the field center, and the *Y*-axis is linear in scaled units. (*b*) Intensity-weighted mean velocity field, obtained by smoothing the maps 5″ spatially and 3 channels in velocity, applying a cutoff of 0.09 Jy beam^{-1} and then integrating the unsmoothed maps over velocities from 655 to 1006 to km s^{-1}. Contours are at 30 km s^{-1} intervals as indicated. Crosses mark the field center (west) and radio continuum peak (east).

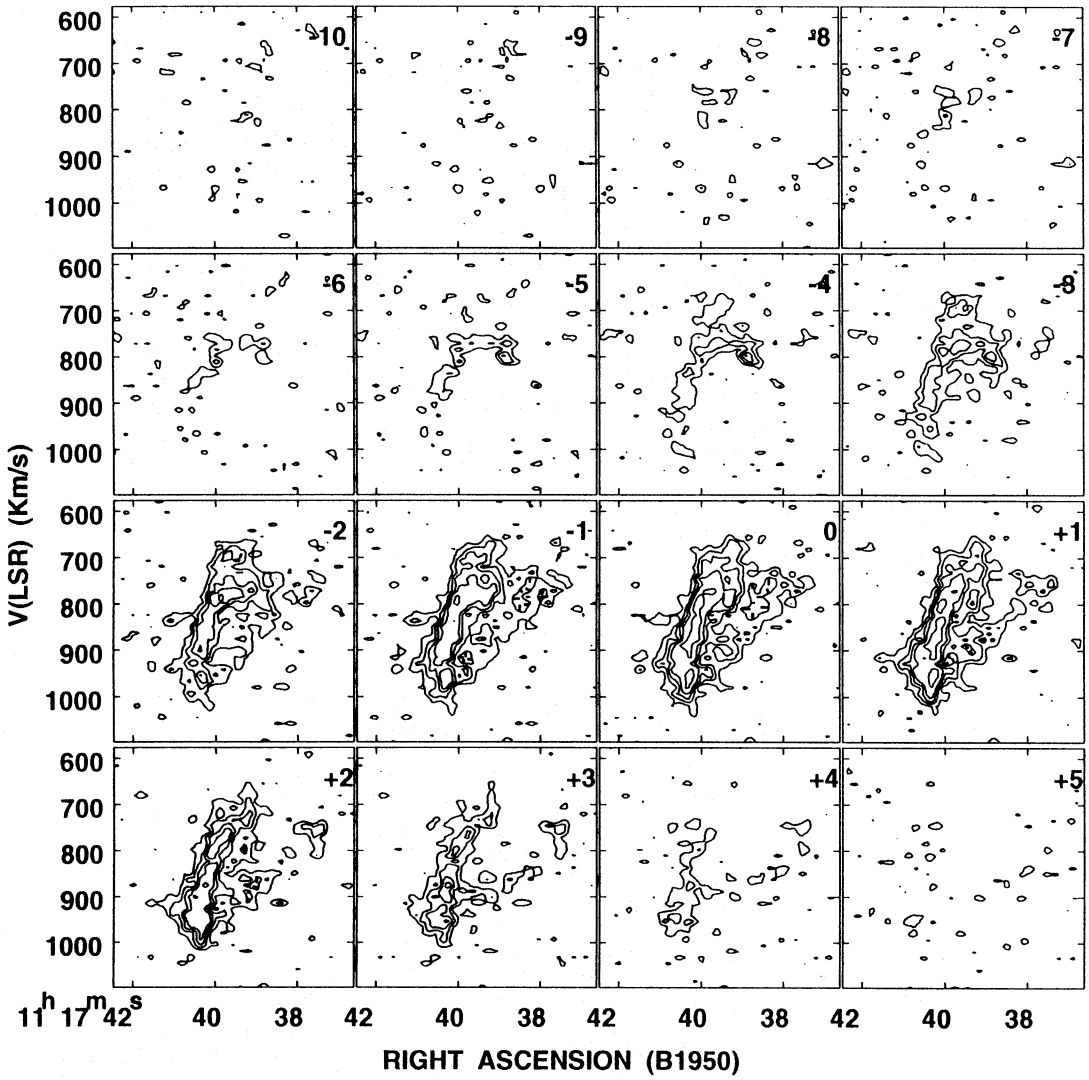

FIG. 5.—Position-velocity plots parallel to the major axis, X, of the galaxy shown at 1″ intervals below and above the plane from $Y = -10''$ (*top left*) to $Y = +5''$ (*bottom right*). Contour levels are as in Fig. 3, and ticks indicate regions of declining intensity.

the kinematics and velocity field of the rotating disk all indicate that the nucleus of the galaxy is located at the radio continuum peak, as defined by the high-resolution (0.″2) 15 GHz emission (Carral et al. 1990). This agrees with the conclusions of Boissé et al. (1987). Note, however, that there is a secondary CO peak at the western location (see Fig. 4*a* inset). With the help of a model, we will fine-tune this nuclear position and systematic velocity (see § 3.8).

Within $X \pm 18''$ (Fig. 6), the strongest emission defined by the brightest components is slightly curved in $X-V$ space. Most of the curvature is on the western (blueshifted) side, indicating that the brightest, most central molecular emission is somewhat asymmetric. At lower contour levels and higher velocities, the emission appears to split into two distinct slopes, shown by the steepest two lines in Figure 6. For example, the steepest slope can be traced from $X = 4.''3$ (140 pc), $V = 211$ km s^{-1} to $X = -3.''6$ (-118 pc), $V = -174$ km s^{-1} and runs through several of the bright knots of emission, including the nucleus. This corresponds to a velocity gradient of 48.7 km s^{-1} arcsec^{-1} = 1.5 km s^{-1} pc^{-1} within a poorly resolved central radius of $\approx 4''$ (130 pc). The second slope can be traced from $X = 16.''7$ (542 pc), $V = 177$ km s^{-1} to $X = -17.''5$ (568 pc), $V = -205$ km s^{-1} and also passes through several bright components as well as the nucleus. This corresponds to a velocity gradient of 11.2 km s^{-1} arcsec^{-1} = 0.34 km s^{-1} pc^{-1} within a diameter of $\approx 17''$ (550 pc).

Two components with different velocity gradients were also found by Baan & Goss (1992) from formaldehyde absorption observations within a smaller central 5″ radius. They find a steep component with a velocity gradient of 1.0 km s^{-1} pc^{-1} and an "anomalous" component with a gradient of 0.29 km s^{-1} pc^{-1}. These slopes are similar to the two CO gradients measured above and may represent the same components, given the different spatial resolutions and regions over which the gradients have been determined. From high-resolution H I absorption data within a 205 pc (6.″3) radius, Schmelz et al. (1987a) found a single velocity gradient intermediate between the above CO values (i.e., 0.83 km s^{-1} pc^{-1}). If we measure the CO slope within an equivalent 205 pc region, we obtain $\approx$0.90 km s^{-1} pc^{-1} (29 km s^{-1} arcsec^{-1}), which is in reasonable agreement. Reuter et al. (1991) derived a lower limit of 0.2 km s^{-1} pc^{-1} for a "fast-rotating disk" within a radius of 225 pc from larger beam single-dish CO(2–1) observations.

We will show (§§ 3.10 and 4.1) that at least some of the complexity observed in the weak emission on the west blueshifted side of the galaxy is due to contributions from

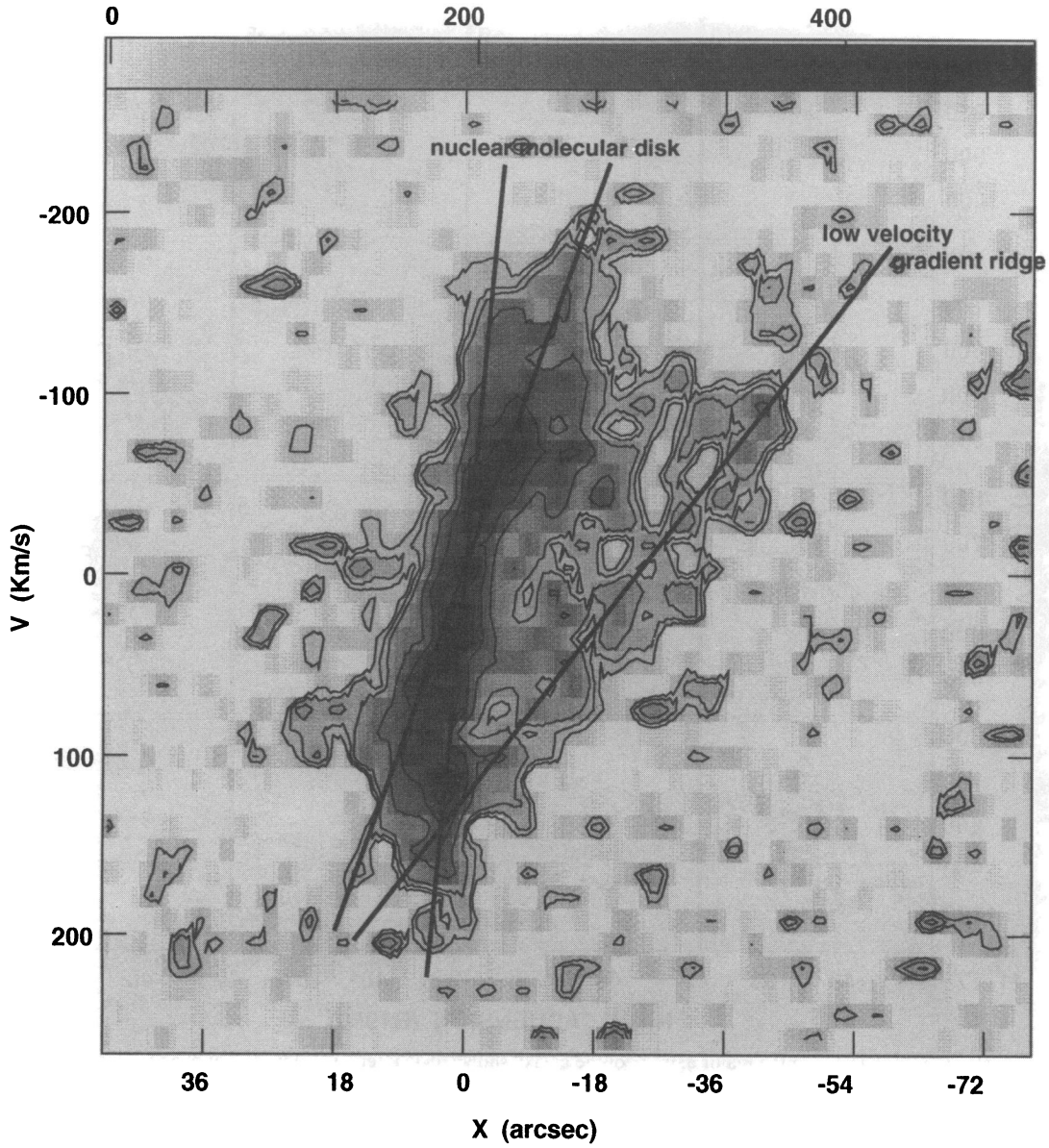

FIG. 6.—Mean position-velocity ($X-V$) plot obtained by averaging over $Y = \pm 5''$ from the galaxy plane. The point (0, 0) corresponds to $11^h17^m40^s.35$ and 840 km s^{-1}. Contours are at 0.05, 0.07, 0.10, 0.20, 0.30, 0.40, 0.50, and 0.55 Jy beam^{-1}, and the gray scale ranges from 0 to 500 mJy beam^{-1}. Two solid lines denote the slopes in the nuclear molecular disk and one solid line denotes the low velocity gradient ridge (see § 3.4).

expanding molecular shells and that there is abundant evidence for starbursting activity within the central 200 pc also. For example, the small horizontal ridge observed at $X = -18''$ to $-27''$, $V = -185$ km s^{-1} is associated with shell D (Table 2). Therefore, it is not clear whether the apparent splitting into two distinct slopes at low intensities is indicating the presence of two separate rotating components, or whether it is due to superimposed components at anomalous velocities in the nuclear vicinity. Whether or not the two components are distinct, the spatial resolution of the CO data is not sufficient to separate them in a more precise fashion. We will therefore treat the inner, bright, high velocity gradient region within $X \pm 17''$ (550 pc) as a single feature, allowing for the possibility of a diminishing velocity gradient with distance from the nucleus. We will refer to this component as "the nuclear molecular disk."

There are other weaker features in the $P-V$ diagram which show lower velocity gradients and extend to radii much larger than 18″. For example, the most easterly emission extends to $X \approx 25''$ (812 pc) and occurs at velocities between $\approx$75–100 km s^{-1}. This emission is also seen in the channel maps (Fig. 3) at 915 km s^{-1}. Several features on the westernmost side of Figure 6 extend out to $X \approx -45''$ (1.5 kpc). These occur over a range of velocities from about -30 km s^{-1} to -180 km s^{-1} and can also be seen in various channel maps (e.g., 746 km s^{-1}). Most of the emission on the western side of the nuclear molecular disk appears "frothy," with many holes suggestive of expanding bubbles. Aside from the bubbly appearance, however, the emission also appears to form a distinct low velocity gradient ridge which is most obvious on the west side of the nucleus and an important contributor to the asymmetry in the total emission noted earlier (see Fig. 4*a*). The low velocity gradient of $\approx$3.94 km s^{-1} arcsec^{-1} = 0.12 km s^{-1} pc^{-1} is still considerably steeper than the steepest gradient of 0.030 km s^{-1} pc^{-1} found by Wilding et al. (1993) for the inner (within approximately a few kpc) H I emission rotation curve. Assuming that the rotation curve gradient declines with

increasing radius over the inner few kpc, this would then imply that the low velocity gradient material of Figure 6 is outside the nuclear molecular disk itself, but within about 1–2 kpc of the nucleus, rather than in foreground or background gas at larger radii. We will refer to this component as the "low velocity gradient ridge" (see Fig. 6). It likely represents an inner spiral arm or portions of a ring or bar (see § 4.3).

3.5. *Clumping, Virial Masses, and the* CO *to* H_2 *Conversion Factor*

Figures 1*a*–1*b*, 3*a*–3*b*, 5, and 6 all illustrate considerable structure in the CO emission down to the smallest spatial scales (i.e., 125 pc) throughout all detectable emission. This indicates that the molecular gas distribution is very clumpy, with the clumps likely representing clouds or cloud complexes. Many clumps, including those with the best signal-to-noise ratio (e.g., peaks along nuclear molecular disk, Fig. 6), tend to occur within a single (binned) velocity channel and therefore have velocity dispersions $\Delta V \lesssim 13$ km s^{-1}. Of the 30 clumps in the channel maps (Figs. 3*a*–3*b*) that are isolated enough for flux measurements (in the range ≈ 1.5–$4\,\sigma$ and unresolved or partly resolved), we have obtained H_2 masses ranging from 5.0×10^5 to $1.3 \times 10^6\ \mathscr{X}\ \mathscr{D}^2\ M_\odot$ with a mean of $9.3 \times 10^5\ \mathscr{X}\ \mathscr{D}^2\ M_\odot$. This is consistent with Reuter et al.'s (1991) conclusion, based on ^{12}CO(2–1) and ^{13}CO(2–1) observations, that the emission is dominated by giant molecular clouds of mass $> 5 \times 10^5\ M_\odot$. Reuter et al. also estimate individual cloud densities to be $n_{H_2} \lesssim 10^4$ cm^{-3}. These clump masses are comparable to those observed in the nearby starburst nucleus of IC 342 ($3 \times 10^5\ M_\odot$ to $2 \times 10^6\ M_\odot$; Downes et al. 1992), but the velocity dispersions are lower than the 30–50 km s^{-1} widths observed for clouds in either IC 342 or the Galactic center (Morris 1995; Downes et al. 1992; Bally et al. 1987).

It is not clear whether the molecular clouds in NGC 3628 are virialized, especially within the high velocity gradient nuclear molecular disk or shell rims (see §§ 4.2 and 4.4). However, if at least some clump masses represent virialized clouds, then we can estimate cloud sizes from the above data. Assuming that there are N identical, constant density spherical clouds within a clump, then $M = N(0.29)R^3\ n_{H_2} = N \times 210 \Delta V^2 R$ (the latter expression from MacLaren, Richardson, & Wolfendale 1988), where M is the total clump mass (including heavier elements), n_{H_2} (cm^{-3}) is the H_2 cloud density, R (pc) is the cloud radius, and ΔV (km s^{-1}) is the internal velocity dispersion of the cloud. Then $R = 27 \Delta V n_{H_2}^{-1/2}$. Using our upper limits for both n_{H_2} and ΔV, we find cloud diameters of order 7 pc. The total H_2 mass of the clump would then be $M_{H_2} \lesssim 8.8 \times 10^4\ N\ M_\odot$. If the clouds are not virialized, then this upper limit should be lower still.

If we now equate the clump masses as determined using the CO $\rightarrow$ H_2 conversion factor to the mass determined from the cloud density upper limit and an assumption of virialization, we have, $M_{H_2} = 5.0 \times 10^5\ \mathscr{X}\ \mathscr{D}^2 \rightarrow 1.3 \times 10^6\ \mathscr{X}\ \mathscr{D}^2 \lesssim 8.8 \times 10^4\ N\ M_\odot$. These values can be reconciled only if $\mathscr{X} \lesssim 0.07$–$0.2\ N\ \mathscr{D}^{-2}$. Since we chose the lowest published value for the distance to the galaxy (§ 1), errors in $\mathscr{D}$ should reduce the estimate of $\mathscr{X}$ even more. That is, if there is one cloud per clump, then the conversion factor for the starburst nucleus of NGC 3628 must be lower than our adopted Galactic value of 3×10^{20} cm^{-2} (K km s^{-1})$^{-1}$ by factors of more than 5–14. This result is consistent with Israel et al. (1990), who suggest a conversion factor for NGC 3628 which is ≈ 6.5 times lower than our adopted value. Sodroski et al. (1995) also estimate conversion factors in the Galactic center to be factors of 3–10 lower than in the Galactic disk. Alternatively, 3–7 clouds within the clump could reconcile $\mathscr{X}$ to the observed range of Galactic values (i.e., ≈ 1.5 to 3.0×10^{20} cm^{-2} (K km s^{-1})$^{-1}$; H. Bloemen, private communication).

The above results are certainly suggestive (though not conclusive) that a lower conversion factor may indeed apply to the nuclear starburst region of NGC 3628. This result is consistent with recent suggestions that different CO $\rightarrow$ H_2 conversion factors may be required for systems experiencing more extreme conditions than typical clouds in the disk of the Milky Way. Nuclear starbursts especially, since they likely have high metallicity, and in which the mean stellar density can exceed the mean gas density (where cloud virialization cannot be assumed), seem to require *lower* conversion factors (Rubio 1995; Sofue 1995; Downes, Solomon, & Radford 1993).

3.6. *A Model of the Nuclear Molecular Disk*

Figures 1*a*–1*b* show that wide, asymmetric and double-peaked profiles are present in the nuclear molecular disk of NGC 3628. Such behavior is sometimes attributed to the presence of extra components and/or components with noncircular velocities. However, it can easily be shown (e.g., Irwin & Seaquist 1991) that a highly inclined and/or thick rotating disk in normal circular rotation can also produce wide, asymmetric, and double-peaked profiles. Therefore, the question arises as to what extent the observed line profiles can be reproduced by a highly inclined circularly rotating disk and to what extent noncircular velocities and/or other components are required.

To answer this question, we modeled the line profiles in NGC 3628 by assuming various density distributions and rotation curves and computing the intensity as a function of velocity at every point of real emission in the cube. This technique was developed by Irwin & Seaquist (1991) and Irwin (1994) and is described fully in these references. It has been used to model the H I distribution in galaxies but is applicable to any gaseous distribution provided that, at any R.A.-decl.-velocity position, $\int I\,dV \propto \int n\,dl = N$, where I is the intensity, dV is a velocity increment, n is the volume density, dl is an incremental line-of-sight distance, and N is the column density. This is true for neutral hydrogen and will also be true for molecular hydrogen, as long as $N_{H_2} \propto I_{CO}$, the only difference being the constant of proportionality. The uncertainty in the conversion factor can be accounted for by noting the dependence of the modeled parameters on $\mathscr{X}$. For this relationship to be valid, we require that the molecular clouds do not shadow each other in position-velocity space. If we consider the intermediate velocity gradient of 0.9 km s^{-1} pc^{-1} measured for the nuclear molecular disk (Fig. 6), the change in velocity over a single beam (125 pc) would then be 113 km s^{-1}, which corresponds to 8.7 independent (binned) velocity channels. Within a single pixel (size 32.5 pc), the change in velocity would be 29.2 km s^{-1}, which corresponds to 2.25 independent velocity channels. Since cloud diameters could be of order 7 pc (§ 3.5), shadowing should not significantly affect the results in the region of the nuclear molecular disk.

For a galactocentric radial coordinate in the galaxy plane, r, and component perpendicular to the plane, z, we

modeled the nuclear molecular disk of NGC 3628 within a radius of 25″ (812 pc). The entire nuclear molecular disk is included in this region as well as some of the low velocity gradient ridge emission on the west side (Fig. 6). Given input density and velocity distributions and trial input parameters, the intensity was calculated at every pixel and then smoothed to the resolution of the synthesized beam. Parameter space was then searched using the Levenberg-Marquardt algorithm until (best-fit) parameters were found which resulted in the minimum residual (data − model) cube. Internal 1 σ errors were also computed for each parameter. For a given combination of density and velocity distributions, this process was repeated for different combinations of initial input parameters to ensure that the routine did not simply iterate to a local minimum in parameter space. All combinations of adopted density and velocity distributions were also tried. These distributions were as follows:

3.6.1. *Radial Density Distribution*

1. Disk of constant density:

$$n(r, z = 0) = n_{\max} .$$

2. Disk centered at galaxy center with exponentially declining density distribution:

$$n(r, z = 0) = n_{\max} \exp\left(-\frac{r}{r_e}\right) .$$

3. Disk centered at galaxy center with Gaussian-like density decline:

$$n(r, z = 0) = n_{\max} \exp\left(-\frac{r^2}{r_g^2}\right) .$$

4. Ring/torus with exponentially declining density from a center at r_0 (scale lengths may be different between the inner and outer sides of ring center):

$$n(r, z = 0) = n_{\max} \exp\left[-\frac{(|r - r_0|)}{r_{e_o}}\right] \quad r \geq r_0 ,$$

$$n(r, z = 0) = n_{\max} \exp\left[-\frac{(|r - r_0|)}{r_{e_i}}\right] \quad r < r_0 .$$

5. Ring/torus with Gaussian-like density decline from a center at r_0 (scale lengths may be different between the inner and outer sides of r_0):

$$n(r, z = 0) = n_{\max} \exp\left[-\frac{(r - r_0)^2}{r_{g_o}^2}\right] \quad r \geq r_0 ,$$

$$n(r, z = 0) = n_{\max} \exp\left[-\frac{(r - r_0)^2}{r_{g_i}^2}\right] \quad r < r_0 .$$

The free parameters are some subset of $n_{\max}$, r_e, r_g, r_0, r_{e_o}, r_{e_i}, r_{g_o}, and r_{g_i}, depending on which distribution is adopted, the maximum number of free parameters being four.

3.6.2. *Perpendicular Density Distribution*

1. Constant density:

$$n(r, z) = n(r, z = 0) .$$

2. Exponential decline centered at midplane:

$$n(r, z) = n(r, z = 0) \exp\left(-\frac{z}{z_e}\right) .$$

3. Gaussian-like decline centered at midplane:

$$n(r, z) = n(r, z = 0) \exp\left(-\frac{z^2}{z_g^2}\right) .$$

There is one free parameter, either z_e or z_g.

3.6.3. *Rotation Curve*

1. Brandt curve:

$$V(r, z) = V(r, z = 0) = V_{\rm sys} \pm \frac{V_{\max}(r/r_{\max})}{[1/3 + 2/3(r/r_{\max})^m]^{3/(2m)}}$$

2. Solid body + flat rotation curve:

$$V(r, z) = V(r, z = 0) = V_{\rm sys} \pm V_{\max} \frac{r}{r_{\max}} \quad r \leq r_{\max} ,$$

$$V(r, z) = V(r, z = 0) = V_{\rm sys} \pm V_{\max} \quad r > r_{\max} .$$

Two different solid body + flat curves were tried corresponding to the two different slopes measured within $r_{\max} = 4''$ and $r_{\max} = 18''$ described in § 3.4.

3. Numerical user-specified rotation curve with amplitude as a free parameter:

$$V(r, z) = V(r, z = 0) = V_{\rm sys} \pm f V_i ,$$

where V_i is measured from Figure 6 at increasing radial distances, r_i.

The maximum number of free parameters describing the velocity distribution is four.

3.6.4. *Galaxy Geometry*

In addition to the parameters describing the density and velocity distributions, four geometrical parameters are required to center and orient the above distributions: the position of the kinematic center of the distribution, R.A.$_0$, decl.$_0$, the position angle of the major axis, P.A., and the inclination of the nuclear molecular disk, *i*.

3.6.5. *Velocity Dispersion*

In the event that the best combination of the above distributions could not reproduce the line widths, a Gaussian velocity dispersion, σ_V, was also included optionally. No attempt was made to model this dispersion as a function of radius. The velocity dispersion is increased systematically by the user until the residuals are minimized.

In total, the number of free parameters is ≤ 14. Within the modeled region, there are 480 independent data points.

3.7. *Model Results*

We present in Table 1 the modeled parameters for a small subset of the various trials, including the best-fit results (trial 4) given in column (5). Column (1) specifies either the form of the distribution or the parameter with units, and columns (2)–(5) list the best-fit results for certain specified distributions. An indication of the adequacy of the fit is given by the last row, which lists the rms of the residual cube over all modeled pixels and shows the improvement in the fit from left (trial 1) to right (trial 4), the latter best fit overall corresponding to an exponential radial density distribution, an exponential vertical density distribution, a Brandt rotation curve, and a velocity dispersion. The rms noise of the input data cube varies with distance from the field center because of the primary beam correction, but an approximate mean value over an equivalent area measured from channels without emission is ≈ 0.093 Jy beam^{-1}.

TABLE 1

MODELED PARAMETERS OF THE NUCLEAR MOLECULAR DISK

Distribution/Parameter (1)	Trial 1 (2)	Trial 2 (3)	Trial 3 (4)	Trial 4 (Best Fit) (5)
$n(r)$	Exponential	Exponential (east side only)	Exponential	Exponential
$n(z)$	Exponential	Exponential	Gaussian	Exponential
$V(r)$	Brandt	Brandt	Brandt	Brandt
Velocity dispersion	No	Yes	Yes	Yes
R.A.$_0$ (B1950)	$11^h17^m40^s.317$	...	$11^h17^m40^s.314$	$11^h17^m40^s.32 \pm 0^s.01$
decl.$_0$ (B1950)	13°51′46″.02	...	13°51′46″.01	13°51′46″.0 ± 0″.1
P.A.	105°.69	101°.36	102°.49	102°.4 ± 0°.2
i	89°.1	85°.5	86°.3	87° ± 1°
V_{sys} (km s^{-1})	843.06	...	841.24	841.3 ± 0.5
V_{max} (km s^{-1})	162.9	164.6	167.1	167 ± 1
r_{max}	1″.47	1″.54	1″.87	1″.89 ± 0″.02
r_{max} (pc)[a]	47.7	49.9	60.7	61.2 ± 0.6
m	0.835	0.990	1.112	1.1 ± 0.2
n_{max} (cm^{-3})[b]	463	983	394	530 ± 150
r_e	5″.53	5″.06	7″.03	7″.01 ± 0″.03
r_e (pc)[a]	180	164.3	228	228 ± 1
z_e	1″.48	1″.53	...	1″.51 ± 0″.06
z_e (pc)[a]	48.1	49.7	...	49 ± 2
z_g	...	...	2″.17	...
z_g (pc)[a]	...	...	70.5	...
σ_V (km s^{-1})	0	36.2	45.2	45.2 ± 0.4[c]
rms (mJy beam^{-1})	124.6	116.9	102.5	101.7

[a] Quantities scale as $\mathscr{D}$.
[b] Quantities scale as $(\mathscr{X}\mathscr{D})^{-1}$.
[c] Uncertainty represents the adopted increment in σ_V.

Consequently, the residual rms after modeling is about 10% higher than the noise, overall. We also formed a ratio cube from the best model cube, using the parameters of column (5) and the input data, applying a 1 σ cutoff to both. The mean model/data ratio over the cube is found to be 0.998, but there are also significant pixel-by-pixel departures from this mean up to a maximum value of 4.0. The residual cube will be discussed in § 3.10.

Some combinations of distribution are not listed, as they resulted in poorer fits overall. For example, constant density in and perpendicular to the plane and combinations with a Gaussian radial density distribution all produced poorer results. Ring/torus distributions also resulted in poorer fits. While Figure 6 shows approximately symmetrically placed intensity peaks on either side of the nucleus, these do not figure strongly in the residual emission once the best model is subtracted off (see Fig. 9), and they more likely represent density enhancements or clumps, rather than indicating the presence of a well-defined ring. The solid body + flat rotation curve does not improve the results and, in any case, it requires an excessive velocity dispersion (i.e., >160 km s^{-1}) to fit the data, since all points along a line of sight in the solid-body case should occur at a single radial velocity (with the exception of line broadening effects due to finite beam size). A rotation curve measured from the envelope of the distribution of Figure 6 also failed to improve the results; the envelope is irregular, highly dependent on which contour it is measured at, and east-west asymmetric, and it is not necessarily a good indication of the global rotation curve.

For examples shown in Table 1, the difference in rms between trial 1 (col. [2]) and trial 4 (col. [5]) illustrates the improvement when a velocity dispersion is included. This improvement is also illustrated in Figures 1*c* and 1*d*, in which we show the same combination of density and velocity distributions without (Fig. 1*c*) and with (Fig. 1*d*) a velocity dispersion.[1] Figure 1*c* clearly shows the predicted double-peaked, wide, and asymmetric profiles expected from a highly inclined disk in pure circular rotation, and it includes any line broadening which is due to the finite size of the synthesized beam. However, even with rotational and beam smoothing effects included, the line widths overall are still too narrow compared to the data (Fig. 1*b*). With the inclusion of a velocity dispersion (Fig. 1*d*), the model line widths are a much better match to the data. The characteristic double peaks are no longer visible, however, having been smoothed over by the Gaussian dispersion. Note that the line profiles of the data (Fig. 1*b*) contain considerable structure which cannot be reproduced by the model (whether or not a velocity dispersion is included), since the model describes only smooth distributions. For example, in the frame at position (8, 4) there is an additional discrete smaller peak on the redshifted side in the data, but not in either model. Structure in the data is retained in the residual emission, which we describe in § 3.10.

Figure 7 shows a comparison between the data and model in the form of position-velocity plots along the major axis of the nuclear molecular disk. The data are shown in gray scale, and the best-fit model (trial 4) is illustrated as contours in Figure 7*a*. The (smooth) model matches the data over the nuclear molecular disk reasonably well, but the model line widths appear slightly broader than the data in this illustration. This is because the model is attempting a fit to all data within ±25″, which also includes a contribution from the low velocity gradient ridge on the western side (§ 3.4). Including some emission from this ridge in the modeled region effectively results in model profiles which are slightly wider than the data profiles appropriate to the

[1] Figs. 1*c* and 1*d* correspond to best-fit results to data which have not been corrected for the primary beam for consistency with Figs. 1*b* and 1*c*. This does not affect our conclusions.

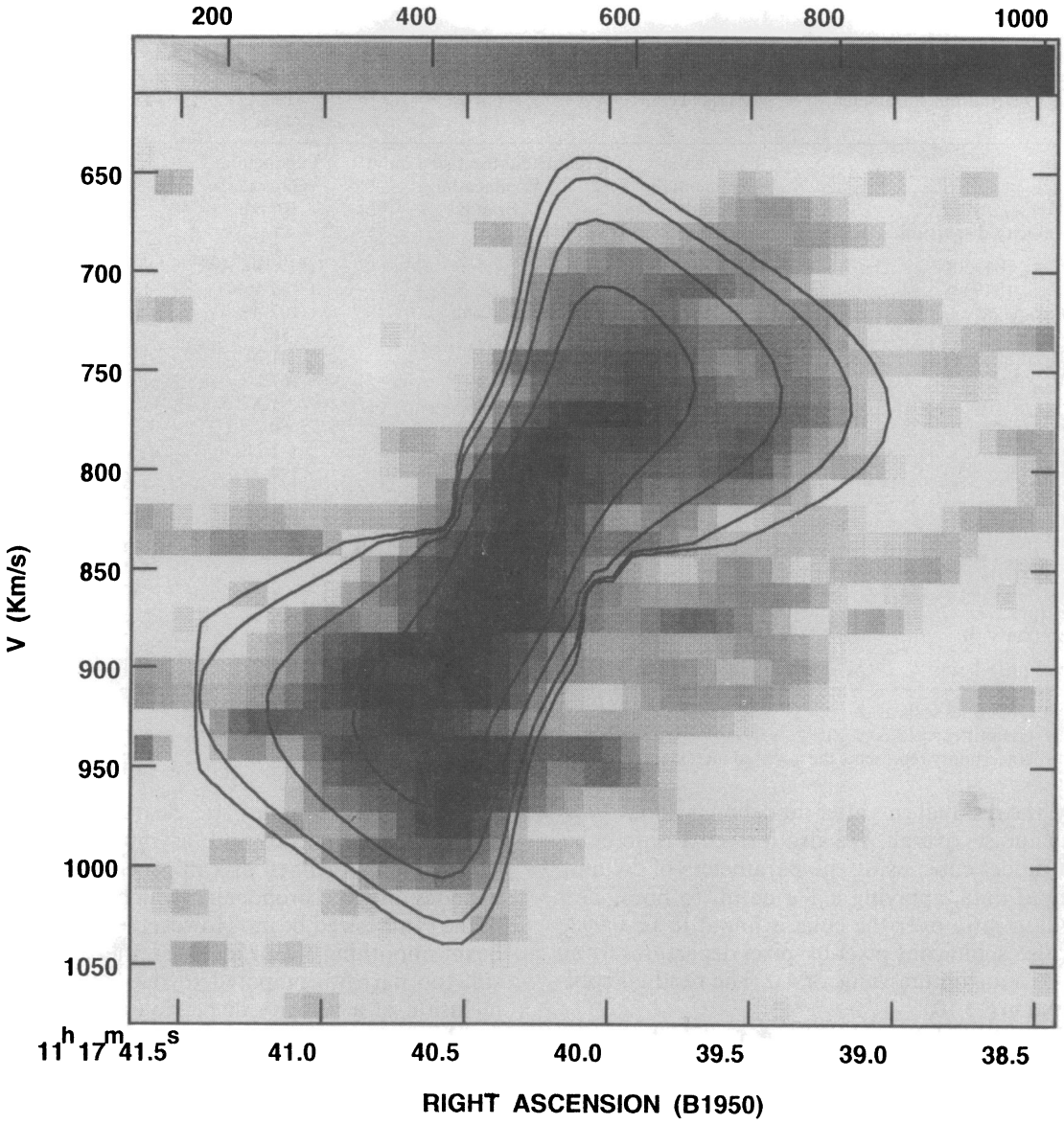

FIG. 7a

FIG. 7.—Position-velocity plots derived from single pixel slices along the major axis of the nuclear molecular disk. In each case, the gray-scale image represents the (primary beam corrected) data, displayed over a range from 0.12 to 1.00 Jy beam^{-1}, and contours show the model at levels, 0.19, 0.25, 0.40, 0.65, and 1.0 Jy beam^{-1}. (*a*) Contours show the best-fit model for the entire nuclear molecular disk, from Table 1, col. (5). The slight truncation on the left side is an artifact of the smoothing code and does not affect the results. (*b*) Contours show the best-fit model for the eastern, receding side only, from Table 1, col. (3).

nuclear molecular disk alone. Therefore, we have also modeled the eastern side of the galaxy alone where the ridge is not seen, fixing the systemic velocity and galaxy center. These results are listed as trial 2 in Table 1 (col. [3]) and are illustrated in Figure 7*b*. The slightly lower velocity dispersion of 36 km s^{-1} (cf. 45 km s^{-1}, col. [5]) results in a closer match to the data on this side.

A comparison between trial 3 (col. [4]) and trial 4 (col. [5]) in Table 1 illustrates that an exponential perpendicular density distribution results in a better fit than a Gaussian perpendicular distribution. This result held consistently over the various trials and velocity dispersions modeled. However, the difference is not large, and the spatial resolution is poor perpendicular to the plane. Consequently, the conclusion of an exponential perpendicular density distribution should be considered tentative. Also, the choice of a Brandt as opposed to some other three-parameter curve also makes little difference to the results. However, a pure solid-body curve can be ruled out because the velocity dispersion required to match the line widths in that case is unrealistically large, and the rms of the residual emission is higher, in any case.

Overall, the best fit resulted from a Brandt rotation curve, an exponential radial density distribution, and an exponential perpendicular density distribution as described by the parameters of Table 1, trial 4, column (5), with the exception that a lower velocity dispersion (i.e., 36 km s^{-1}) is likely a better descriptor of the internal velocity dispersion in the nuclear molecular disk itself.

3.8. *Parameters of the Nuclear Molecular Disk*

Most of the parameters of Table 1 are robust in the sense that they model to virtually the same value, independent of choice of density or velocity distribution. This was also

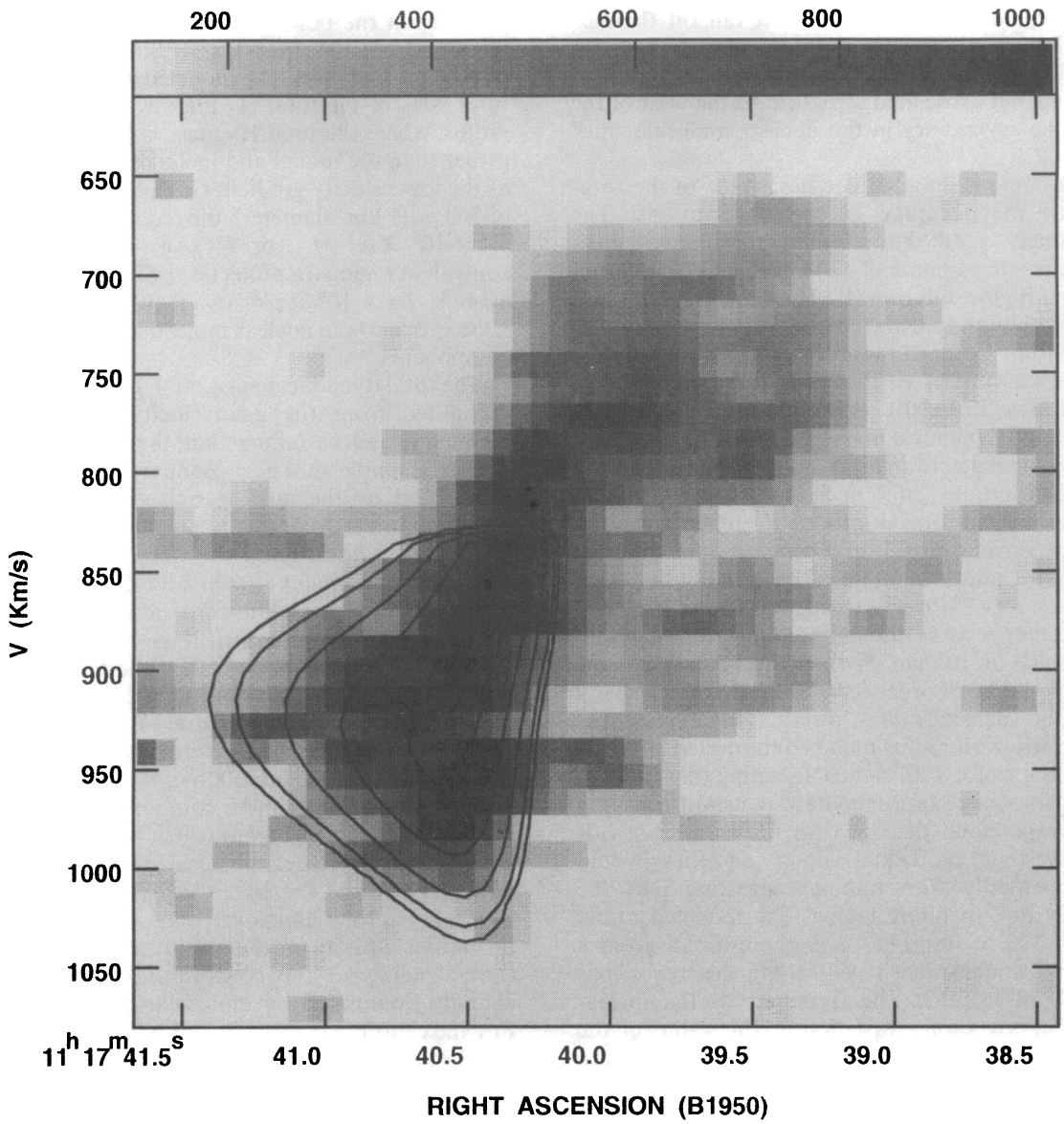

FIG. 7*b*

usually true of discarded models (e.g., those with a ring or Gaussian radial density distribution or those with different velocity dispersions). We list, in column (5), an estimate of the uncertainties on each parameter, which reflect either 1 σ internal errors or variations over good models, whichever is larger. These errors do not include any systematic effects, such as those which might result from the insensitivity of the interferometer to broad spatial scales, nor do they include differences between the advancing and receding sides of the disk which are occasionally significant because of the asymmetry observed in the emission (e.g., cf. r_e, n_{max} for the east side, col. [3], compared to both sides, col. [5] of Table 1).

The kinematic center, in particular, is determined quite precisely and can be compared with the radio continuum peak of Carral et al. (1990). We find the kinematic center to agree with the position of two brightest 15 GHz peaks (their C7 and C8) to within a fraction of an arcsecond. The position angle of the major axis consistently models to $\approx 102°$, which agrees with the position angle of the larger scale neutral hydrogen distribution of $103\overset{\circ}{.}6 \pm 1\overset{\circ}{.}7$ (Wilding et al. 1993), and is close to the 1.49 GHz position angle of 104° (Condon 1987) as well as the optical position angle of 104° (Nilson 1973). The inclination of the nuclear torus is almost edge-on, at 87°. Boissé has suggested earlier, from previous ^{12}CO single-dish data, that the inclination should be $>86°$, and Roberts (1975) finds an optical inclination of 89°. The lower value of $79\overset{\circ}{.}9$ for the broad scale neutral hydrogen, as pointed out by Wilding et al. (1993), is due to their use of the intensity weighted mean velocity field, rather than the line profiles, to model the inclination of an edge-on galaxy. The systemic velocity of 841 km s^{-1} is also in excellent agreement with H I values (843 km s^{-1}, Tifft & Cocke 1988; 841 km s^{-1}, Wilding et al. 1993) and our previous measurement from the global profile (841 km s^{-1}). In summary, the kinematic center of the nuclear molecular disk corresponds to the radio continuum peak, and its position angle, inclination, and systemic velocity are virtually identical to those of the large-scale stellar and gaseous distributions. This agreement between nuclear and large-scale geometry is interesting, considering the asymmetries observed in overall galactic structure and in the molecular emission observed

here. These include the substantial tidal tail on the east (Rots 1978; Haynes et al. 1984), the warp at large radii on the west (Wilding et al. 1993), the low velocity gradient molecular ridge and associated structure to the west of the nucleus, and the asymmetry in the nuclear molecular disk itself.

The Brandt curve is an adequate descriptor of the rotation curve, to the accuracy of the observations. The maximum velocity of 165 km s^{-1} is in reasonable agreement with the rough estimate of 170 km s^{-1} by Schmelz et al. (1987a) from high-resolution (1″) H I data, and with half the velocity width found for the central H I absorption (i.e., 175 km s^{-1}) within a central radius of 244 pc by Wilding et al. (1993). The curve rises to this peak quite rapidly, i.e., within several arcseconds, suggesting a fairly strongly centrally concentrated dynamical mass (see § 3.9).

The quantitative determination of n_{max} is less secure because of the uncertainty in $\mathscr{X}$ and also because fitting an exponential to the central peak produced greater variation in n_{max} over the various models and between different sides of the disk. If we adopt a range of central density from $n_{max} = 394\ cm^{-3}\ \mathscr{X}\mathscr{D}^{-1}$ (trial 3) to $n_{max} = 983\ cm^{-3}\ \mathscr{X}\mathscr{D}^{-1}$ (trial 2) and Reuter et al.'s (1991) upper limit to an individual cloud density of $10^4\ cm^{-3}$, then the central volume filling factor should be of order 0.04–0.1 $\mathscr{X}\mathscr{D}^{-1}$ (or larger if individual cloud densities are lower). The exponential decline in intensity with radius may be interpreted either as a decline in filling factor with radius assuming that individual cloud densities are approximately constant, or as a decline in average cloud density with radius, or both. It seems unlikely that individual cloud densities would decrease exponentially with radius, suggesting that the effect is largely due to filling factor. The modeled radial scale length of 228 pc improves over the estimate from a single one-dimensional intensity cut along the major axis (290 pc, Fig. 4*a*, inset, § 3.3). The asymmetry in the nuclear disk, however, imposes some variation on this value; cf. the scale length of 164 pc on the east side only. These values are similar to the size of 205 pc estimated by Schmelz et al. (1987) from their H I absorption velocity gradient and their rough estimate of V_{max}. The similarity in both r_e and V_{max} between the H I and CO suggests that the neutral and molecular gas are roughly coexistent within the central few hundred pc of NGC 3628.

There has been no previous measurement of the thickness of the nuclear molecular disk which we find to have an exponential scale height of 49 pc or a Gaussian (trial 3) σ_z of 50 pc [$\sigma_z = (z_g/2)^{1/2}$]. Therefore, the disk thickness is approximately 20% of its diameter.

A velocity dispersion of 45 km s^{-1} (FWHM = 108 km s^{-1}), a significant fraction of the rotational velocity, is required to match the data, overall, though a smaller value of 36 km s^{-1} is more appropriate for the east side alone. This dispersion includes any noncircular velocity in the line-of-sight coordinate which could widen the line profiles, for example, motions within clouds as well as between clouds. Since clouds appear to have dispersions $\lesssim$13 km s^{-1}, σ_V must be largely due to the dispersion *between* clouds.

3.9. *The Nuclear Disk*: H_2 *Mass, Dynamical Mass, and Mass Fraction*

The mass of the nuclear molecular disk alone, without foreground or background contamination, can be computed from the best-fit model. We find a nuclear disk H_2 mass of $2.9 \times 10^8\ \mathscr{X}\mathscr{D}^2\ M_\odot$ within one scale length of 228 pc (456 pc diameter). The modeled nuclear disk mass constitutes 90% of the total H_2 mass within the same projected radius, where the total H_2 mass is calculated from the data rather than the model and includes other components such as the low velocity gradient ridge. Similarly, within a radius of 500 pc (1 kpc diameter), the modeled nuclear disk mass is $4.4 \times 10^8\ \mathscr{X}\mathscr{D}^2\ M_\odot$, or 84% of the total H_2 mass in the equivalent region (in projection). Since the total detected H_2 mass is $7.4 \times 10^8\ \mathscr{X}\mathscr{D}^2\ M_\odot$ (§ 3.1), most of the detected mass is due to the nuclear molecular disk, rather than other components.

The total dynamical mass, $M_T(r)$, within a radius r, can be computed from the gas velocity, $V(r)$, assuming some geometry, and assuming that the gas is bound. Here we choose a simple spherical geometry, since the mass is likely dominated by the nuclear bulge, in which case $M_T(r) = rV(r)^2/G$. In the event that the region is better described by a flat disk, the total mass will decrease by no more than a factor of 2 (Lequeux 1983). The determination of bound velocities is not straightfoward, however, because the velocity dispersion is significant. If we assume that only gas in circular rotation is bound, then the total dynamical mass can be computed from the modeled rotation curve which excludes the velocity dispersion. In this case, we find a total mass of $8.9 \times 10^8\ \mathscr{D}\ M_\odot$ within a radius of 228 pc and $1.1 \times 10^9\ \mathscr{D}\ M_\odot$ within 500 pc. If all velocities are bound, then the total mass can be computed from the envelope of the $X-V$ diagram (Fig. 6) which includes the velocity dispersion. In this case, the total mass is $1.6 \times 10^9\ \mathscr{D}\ M_\odot$ within 228 pc and $4 \times 10^9\ \mathscr{D}\ M_\odot$ within 500 pc.

The H_2 to total dynamical mass ratio has been computed by various authors for the central regions of galaxies, sometimes leading to the conclusion that the total mass is actually dominated by molecular gas (e.g., Turner 1994). For the central 228 pc radius of NGC 3628, we find a ratio of $33\mathscr{X}\mathscr{D}$% if only gas in circular motion is bound, or $18\mathscr{X}\mathscr{D}$% of the total mass if gas at all velocities is bound. Therefore, molecular hydrogen is a significant, but not dominant component of the dynamical mass within the inner few hundred pc of NGC 3628.

3.10. *The Residual Emission: Expanding Molecular Shells*

When the model cube is subtracted from the data, a residual cube is formed which can be inspected for anomalous velocities and densities which could not be fitted by circular rotation and smooth density distributions. From this residual cube, we have formed a map (Fig. 8) which has been averaged over velocity and whose origin (0, 0) has been placed at the modeled center (Table 1, col. [5]). Positive contours indicate regions of excess emission, while negative contours indicate an absence of emission in comparison with the model. Since the radial scale length of the nuclear molecular disk is only 7″ and the perpendicular scale length is only 1″.5, the effects of the model subtraction become quite small beyond these radii, and virtually *any* of the models tried could have been subtracted from the data with similar results, i.e., the residual features discussed below are not strongly dependent on the details of the model. An $X-V$ slice averaged over strips parallel to the major axis has also been formed from the residual cube (see Fig. 9).

The residual emission is complex, but the most obvious features appear arc- or bubble-like. Many of these features

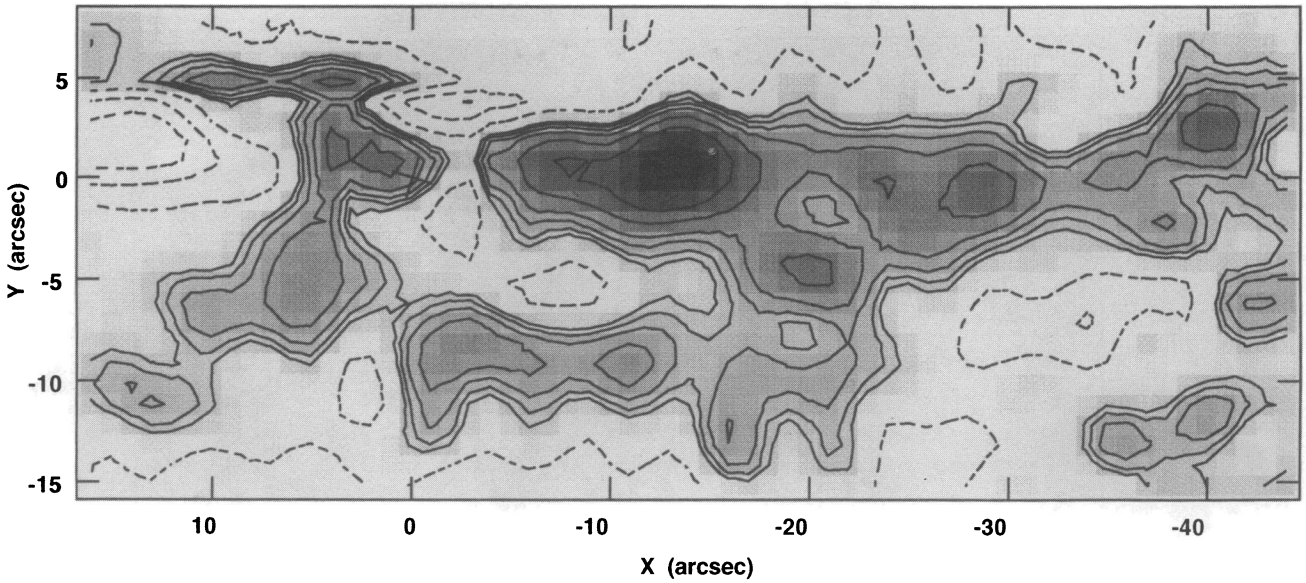

FIG. 8.—Average of the residual (data − model) cube over the velocity range 630 km s^{-1} to 1071 km s^{-1}, in the $X-Y$ plane. The center (0, 0) is marked with a cross and has been placed at the modeled center (Table 1, col. [5]). Contours are at −50, −32, −10, 10, 15, 22, 32, 50, 75, and 120 mJy beam^{-1}, and the gray scale ranges from 0 to 120 mJy beam^{-1}.

merge or overlap in various $X-Y$, $X-V$, or $Y-V$ diagrams. The extraplanar arcs are seen mostly toward the south (i.e., $Y < 0$) of the plane, as observed earlier in Figures 3 and 4, and they can be traced to z of at least 13″ (430 pc) in projection. The extensions appear to originate at various positions along the plane rather than from a single origin, consistent with distributed energetic activity rather than a compact nuclear core. From the $X-V$ plot (Fig. 9), it is clear that most of the residual emission either falls along or centers on the low velocity gradient ridge (i.e., $X = 4''.5$, $V = 120$ km s^{-1} to $X = -45''$, $V = -100$ km s^{-1}). The ridge consists of gas which is exterior to the rapidly rotating nuclear molecular disk but is probably within a few kpc of the nucleus (§ 3.4).

While the residual features tend to be blended and complex, several are relatively distinct and appear to form arcs or circles in $X-Y$, $X-V$, and/or $Y-V$ space. Such signatures are characteristic of expansion (although technically contraction is indistinguishable). We have identified four features which show circular structure in $X-Y$, $X-V$, and/or $Y-V$ space. These are listed in Table 2 along with their central positions and velocities (cols. [2], [3]), their total velocity extent, ΔV (col. [4]), radii, R (col. [5]), and masses, M (col. [6]). The latter quantity is the most uncertain due to its dependence on $\mathscr{X}\mathscr{D}^2$ and the difficulties in isolating all the emission associated only with the particular feature. We have also estimated an expansion energy, E (col. [7]) via $E = \frac{1}{2} M (\Delta V/2)^2$, as well as a characteristic timescale, τ (col. [8]) via $\tau = 2R/\Delta V$. The energies should only be considered order of magnitude estimates and the timescales will be upper limits, since deceleration is not included. The dependence of these quantities on $\mathscr{X}$ and $\mathscr{D}$ are given in the notes to the table. The four features are discussed below.

The most prominent feature in both $X-Y$ and $X-V$ diagrams (Figs. 8, 9) is a strong peak of emission on the major axis at $X = -13''$. This position corresponds to the secondary peak shown in the inset to Figure 4*a* and is approximately at the IRAM CO(2–1) peak. As the $X-V$ plot illustrates (consider a vertical line along $X \approx -13''$), this is not a single feature, but it is rather the sum of several different components over a wide range of velocity. The strongest of the components is roughly circular about a small "hole" centered at a velocity of $\approx +55$ km s^{-1} [V(LSR) = 895 km s^{-1}] and can also be seen, though less obviously, in the $X-V$ diagram of the total emission before the model has been subtracted (Fig. 6). This feature is denoted A (Table 2).

Feature B is another small ring of emission embedded in the low velocity gradient ridge, centered in Figure 9 at $X \approx -33''$ and a velocity of −62 km s^{-1} (778 km s^{-1}). This feature also forms a partial arc when plotted in $Y-V$ space (not shown). It is situated at a minimum on the major axis

TABLE 2

EXPANDING MOLECULAR SHELLS

Feature (1)	Center X, Y, V[a] (2)	Center R.A., Decl., V_{LSR}[a] (3)	ΔV (total) (km s^{-1}) (4)	R[b] (pc) (5)	M[c] ($M_\odot$) (6)	E[c] (ergs) (7)	τ[b] (yr) (8)
A.....	−13″, 0″, +55	11^{h}17^{m}39^s.5, 13°51′50″, 895	40	139	6.7×10^6	2.7×10^{52}	$<6.8 \times 10^6$
B.....	−33, −1, −62	11 17 38.1, 13 51 54, 778	65	107	6.4×10^6	6.8×10^{52}	$<3.2 \times 10^6$
C.....	−13, 0, 55	11 17 39.5, 13 51 50, 895	299	600	$>1.1 \times 10^7$	$>2.5 \times 10^{54}$	$<3.9 \times 10^6$
D.....	−20, −5, −126	11 17 38.9, 13 51 47, 714	169	253	1.7×10^7	1.2×10^{54}	$<2.9 \times 10^6$

[a] V (col. [2]) and V_{LSR} (col. [3]) are given in units of km s^{-1}.
[b] Quantities scale as $\mathscr{D}$.
[c] Quantities scale as $\mathscr{X}\mathscr{D}^2$

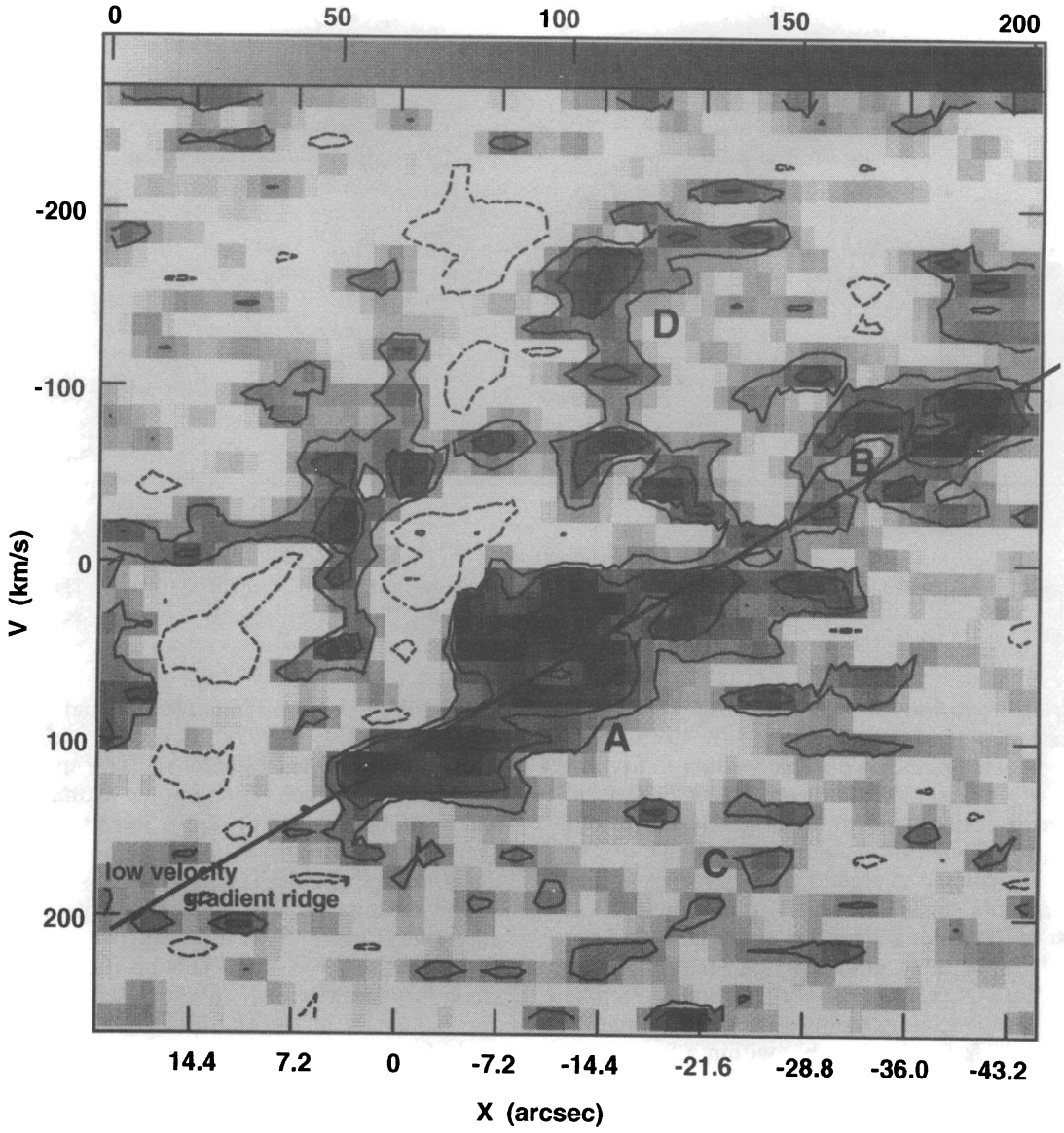

FIG. 9.—Position-velocity ($X-V$) slice parallel to the major axis of the residual (data − model) cube. The data have been averaged over a strip 9″ wide in the Y coordinate centered 1″ to the south of the major axis. Contours are at −175, −130, −80, 50, 100, 175, and 250 mJy beam^{-1}, and the gray scale ranges from 0 to 200 mJy beam^{-1}. A solid line denotes the low velocity gradient ridge, and the four residual loops A–D are indicated (see § 3.10).

in Figure 8 with brighter emission on either side along the plane. It is also bracketed by two extensions toward the north (positive Y) of the plane, suggesting that gas may have escaped in this direction.

In the $X-V$ plot along the major axis, there is a second feature whose origin is at the origin of feature A, i.e., at $X = -13''$ and $V = +55$ km s^{-1} (895 km s^{-1}), but it is considerably larger, forming a ring around this position over a total velocity spread of 299 km s^{-1} and extending from $X \approx 5''$ to $X \approx -32$ km s^{-1}. We denote this feature C. South of the plane (Fig. 8), the strongest emission forms a large clumpy arc roughly parallel to the major axis along $Y \approx -8''$, stretching from $X \approx 5''$ to $X \approx -20''$ where it appears to blend with other features. An $X-V$ plot along this arc shows weak clumpy emission in a ring pattern centered at $V = 895$ km s^{-1}, $X = -5''$ and with a total velocity spread of 272 km s^{-1}. The similarity in central velocity, total velocity spread, and size between the off-major axis arc and the major axis feature would suggest that these are parts of the same expanding shell, the southern arc having a slightly smaller total velocity spread and radius because it is centered away from the plane, slices are not taken through the shell center. There is also a 5″ shift in X between the southern and major axis ring centers, suggesting some bulk motion toward the east with distance from the plane. In Table 2, the computed mass of feature C is a lower limit, since only a fraction of the mass could be isolated for this measurement.

The final feature, feature D, is associated with the complex looplike emission in and south of the plane about 20″ to the west of the nucleus (Fig. 8). In the $X-V$ slice along the plane (Fig. 9), this feature shows up as a half-circle centered at $X \approx -20''$ and $V \approx -126$ km s^{-1} (714 km s^{-1}). A $Y-V$ slice through this feature is shown in Figure 10 and displays a clear ring shape centered just south ($Y \approx -5''$) of the major axis. This shell is centered at the apex of the velocity cone in Figure 4*b* and is the best example of an expanding shell in these data.

4. DISCUSSION

The CO emission in the nuclear region of NGC 3628 is dominated by three main components: (*a*) a rapidly rotating centrally concentrated

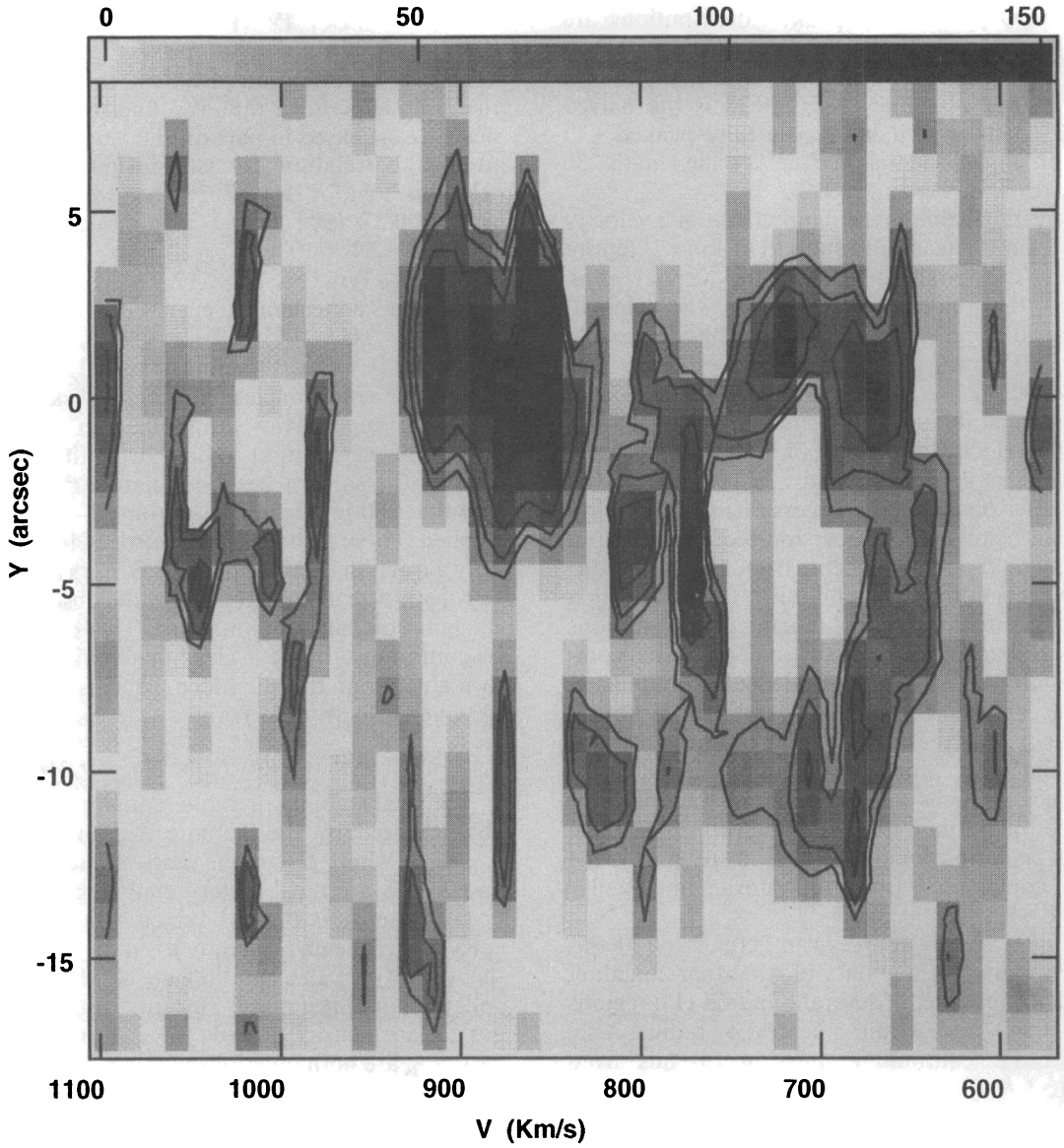

FIG. 10.—$Y-V$ plot perpendicular to the major axis of the residual (data − model) cube averaged over 14″ centered at a position $X = -19''$, displaying expanding shell D. Contour levels are at 40, 60, 90, 150, and 220 mJy beam^{-1}, and the gray scale ranges from 0 to 150 mJy beam^{-1}.

at the nucleus, (*b*) a lower intensity low velocity gradient ridge, mostly visible to the west of the nucleus, and within a few kpc of it, and (*c*) complex, blended expanding molecular shells, mostly (but not entirely) centered on the low velocity gradient ridge, with some extensions out to 430 pc from the plane. In addition, the emission is very clumpy throughout, both within the nuclear molecular disk, as well as in the molecular shell rims. These components, as well as star formation and comparisons with data at other wave bands, will be discussed below.

4.1. *The Nuclear Molecular Disk and Energy Input*

This component can best be modeled as a highly inclined ($i = 87°$) rapidly rotating disk centered at the strongest radio continuum emission which is at the nucleus of the galaxy. The optical center lies 11″ from the nucleus toward the west, likely displaced because of obscuration. The far-IR peak is offset 19″ to the east of the nucleus (see Boissé et al. 1987), but as pointed out by Israel et al. (1990), the 12 μm peak is actually coincident with the radio nucleus. The disk is strongly centrally concentrated with considerable substructure, and there is no compelling evidence for a ring/torus distribution within a radius of $\approx$500 pc. The best-fit model suggests that the mean density falls off exponentially in both the radial and perpendicular directions with scale lengths of about 230 pc and 50 pc, respectively, suggesting that the disk thickness is about 20% of its diameter. An estimate of the maximum volume filling factor at the center is $\approx$0.04–0.1 $\mathscr{X}\mathscr{D}^{-1}$ (or larger if individual cloud densities are lower). This value decreases with radius and height if the exponential decline in mean density represents a decline in filling factor.

There are still few galaxies whose CO distributions have been observed with 125 pc resolution or better. Some nearby examples are IC 342, in which a molecular bar resolves into curved ridges with a central hole (Ishizuki et al. 1990), and the prototypical starburst galaxy, M82, which shows off-nuclear CO peaks at a radius of about 200 pc (Nakai et al. 1987; Carlstrom 1988). Barred galaxies, especially, tend to show ring/torus distributions or "twin peaks" which have been interpreted as crowding at inner Lindblad resonances in the presence of a barred potential

(Kenney et al. 1992). Centrally peaked distributions are rarer, though the relative absence of central peaks may, to some extent, result from beam dilution. One example of a galaxy which closely resembles NGC 3628 is the barred starburst, NGC 3504, which has a centrally peaked CO distribution with an exponential decline of scale length 230 pc (Kenney, Carlstrom, & Young 1993).

A rather interesting result is the requirement of a velocity dispersion of 36 km s^{-1} (east side only) to 45 km s^{-1} (entire region), which is supersonic in most media. Kenney et al. (1993) modeled the velocity dispersion in the (almost) face-on nuclear disk of NGC 3504, finding decreasing values from 47 ± 9 km s^{-1} at the center to 13 ± 2 km s^{-1} at a radius of 600 pc. Consequently, the mean dispersion in NGC 3628 is comparable, possibly slightly higher than in NGC 3504. The velocity dispersion in NGC 3628 largely represents motions between clouds, since unresolved clumps have rather low velocity dispersions (i.e., <13 km s^{-1}, see § 3.5 and below). This dispersion requires an input of energy which could potentially arise from turbulence due to instabilities, expanding shells/bubbles, large-scale systematic expansion/contraction, noncircular motions resulting from a bar or oval distortion, or some combination of the above. We see no evidence for systematic motions such as expansion/contraction, and there is no evidence for a bar within the inner region occupied by this nuclear molecular disk. Since NGC 3628 is a starburst, expanding molecular shells are present, and there is compelling evidence for outflow from the nuclear vicinity, the most natural explanation for the velocity dispersion is the kinetic energy contributed from supernovae and stellar winds associated with the starburst.

Indeed, the input energy sources can actually be identified. Radio recombination line data of Anantharamaiah et al. (1993) imply the presence of several hundred H II regions and several $\times 10^4$ O stars within a central 5″ radius. Also, the strongest radio continuum emission extends from $\approx 11^h17^m39^s.8$ to $11^h17^m40^s.8$, or $\approx 15''$ (see image of Condon et al. 1990), which coincides with the extent of the nuclear molecular disk, and the strongest central emission resolves into numerous individual radio continuum components (Carral et al. 1990), i.e., radio continuum sources are embedded throughout the disk. Most of these sources are nonthermal (Anantharamaiah et al. 1993), likely radio supernovae.

It is interesting to consider whether the energy input associated with these sources is sufficient to produce the observed velocity dispersion. The H_2 mass of the entire nuclear molecular disk is $3 \times 10^8\ \mathscr{X}\mathscr{D}^2\ M_\odot$ (§ 3.9), with a scale length of 7″ or 228 pc.[2] If we make the rough approximation that every cloud in the nuclear molecular disk is moving at the dispersion velocity of $\sigma_V \approx 40$ km s^{-1}, then the kinetic energy associated with agitating the entire disk to this velocity is $\approx 5 \times 10^{54}\ \mathscr{X}\mathscr{D}^2$ ergs. Within a slightly smaller central 5″ (160 pc) radius, Condon et al. (1982) find a 1.4 GHz radio continuum flux density of 191 mJy. Since Anantharamaiah et al. (1993) estimate the nonthermal contribution to the total radio continuum flux to be 80% at 5 GHz, the nonthermal contribution at 1.4 GHz, S_{NT}, must be in the range 80%–100% i.e., $153 \leq S_{NT}$ (mJy) ≤ 191. This corresponds to a nonthermal radio luminosity, L_{NT}, of $8.2 \times 10^{20} \leq L_{NT}$ (W Hz^{-1}) $\leq 1.0 \times 10^{21}$ $(\mathscr{D}^2)$. Condon (1992) has provided relations connecting the massive (i.e., $\geq 5\ M_\odot$) star formation rate, SFR, the FIR luminosity, L_{FIR}, the radio supernova rate, ν_{SN}, and nonthermal radio luminosity, L_{NT}, based in part on the empirical FIR–radio continuum correlation for star-forming galaxies. If these relations hold for NGC 3628, then we find $0.22 \leq$ SFR ($M_\odot$ yr^{-1}) ≤ 0.27 $(\mathscr{D}^2)$ (using a nonthermal spectral index, $\alpha = -1$), $2.4 \times 10^9 \leq L_{FIR} \leq 3.0 \times 10^9$ $(\mathscr{D}^2)$, and $9.0 \times 10^{-3} \leq \nu_{SN}$ (yr^{-1}) $\leq 1.1 \times 10^{-2}$ $(\mathscr{D}^2)$. If each radio supernova inputs a mechanical energy of 10^{51} ergs, then an input rate, $\mathscr{E}$, of $9.0 \times 10^{48} \leq \mathscr{E}$ (ergs yr^{-1}) $\leq 1.1 \times 10^{49}$ $(\mathscr{D}^2)$ is available. It would therefore take only $4–6 \times 10^5\ \mathscr{X}$ yr to agitate the entire nuclear molecular disk from the input of the radio supernovae within the central 5″ alone. Other sources of energy input could shorten this timescale.

Over the same 5″ region, Anantharamaiah et al. (1993) find that 280 H II regions and some $3–7 \times 10^4$ O5 stars are implied. These O stars are a source of future supernovae. If only a fraction ($<10\%$) of these O stars are being converted to supernovae at any given time, the observed level of velocity agitation can be maintained. This process is unlikely to be continuous, but it is clear that sufficient energy input is available from the identified sources to account for the observed velocity dispersion.

4.2. *Local Stability in the Nuclear Molecular Disk*

The local stability of a differentially rotating disk is often characterized by the Toomre instability parameter, $Q = \Sigma_{crit}/\Sigma_{gas}$, where Σ_{gas} is the mass surface density of the gas and Σ_{crit} is a critical surface density given by $\Sigma_{crit} = \sigma_V \kappa/(\pi G)$. Here σ_V is the gas velocity dispersion and κ is the epicyclic frequency, given by $\kappa^2 = 2V/r\,(V/r + dV/dr)$, V is the velocity of the rotation curve at radius r. Localized collapse (and presumably star formation) can proceed if the gas surface density exceeds the critical value, i.e., if $Q < 1$. As κ, Σ_{gas} are both functions of radius, Q is as well.

The gas surface density is determined by $\Sigma_{gas} = 1.4(\Sigma_{H_2} + \Sigma_{H\,I})$, where the factor, 1.4, takes heavy elements into account. For NGC 3628, we can compute the H_2 surface density (as if looking at the galaxy face on), using the quantities in Table 1, column (5). For a central volume density of $530\ \mathscr{X}\mathscr{D}^{-1}$ cm^{-3} and scale height of $49\mathscr{D}$ pc, we find $\Sigma_{H_2} = 2.6 \times 10^3\ \mathscr{X}^{-1}\ M_\odot$ pc^{-2}. For a constant scale height, this value then decreases exponentially, such that at one scale length (228 pc) the value is $9.4 \times 10^2\ \mathscr{X}^{-1}\ M_\odot$ pc^{-2}. There is a 35% uncertainty on these values.

$\Sigma_{H\,I}$ for the nuclear disk is difficult to estimate from the available literature because the H I is absorbed against the nuclear continuum, requiring an estimate of spin temperature, T_S, and also because it is difficult to isolate the H I in the nuclear regions alone without contamination from foreground or background gas. Schmelz et al. (1987) have identified 10 H I absorption components each of $\approx 10^5\ M_\odot$ (assuming $T_S = 100$ K) which, from position-velocity plots, appear to be in the nuclear region within a radius of $\approx 2''.8$. This places a lower limit (because of spatial filtering) of $10^6\ M_\odot$ on the H I in this region. Within the same radius, our H_2 mass, determined from the best-fit model, is $6.5 \times 10^7\ \mathscr{D}^2\ \mathscr{X}\ M_\odot$, suggesting that the neutral component constitutes only $>1.5\%$ of the H_2 mass in this region. It is not known whether this ratio holds over the entire nuclear molecular disk, but if so, then $\Sigma_{H\,I}$ is a negligible contributor to the total gas surface density. Therefore, we find $\Sigma_{gas} =$

[2] For the accuracy of this calculation, it is not necessary to include the mass of He.

$3.7 \times 10^3\ \mathscr{X}^{-1}\ M_\odot\ \mathrm{pc}^{-2}$ at the center, decreasing to $1.3 \times 10^3\ \mathscr{X}^{-1}\ M_\odot\ \mathrm{pc}^{-2}$ at one scale length.

We have computed Q at four positions: near the nucleus (i.e., $r = 16$ pc), at the peak of the rotation curve, $r = 61$ pc, at one radial scale length, $r = 228$ pc, and at two radial scale lengths, $r = 456$ pc. We find values of Q in the range 12–1.2 (values decreasing with increasing r), where the range includes the uncertainty in σ_V. This suggests that the gas density is insufficient to be locally self-gravitating in the presence of a velocity dispersion of order 36–45 km s^{-1}. This conclusion depends upon the assumption that the disk can be approximated as uniform (at some r) and thin. In fact, this is not the case within about one radial scale length, since the "most unstable wavelength," λ (see Binney & Tremaine 1987), falls below twice the vertical scale height, $2z_e$, in this region, and the density also changes significantly over a vertical height of size λ. Consequently, a three-dimensional analysis is really required, which is beyond the scope of this paper. From this approximation, however, it would appear that the disk is too agitated for local instabilities to grow. On the other hand, condensations are indeed observed throughout the disk, so it may be that processes other than self-gravity are forming them. For example, the energy input from star-forming processes, while keeping the disk agitated, could also be actively compressing the gas in shocks and at local boundaries.

4.3. *The Low Velocity Gradient Ridge: Is* NGC 3628 *Barred?*

The low velocity gradient ridge (see Figs. 6 and 9) extends to about 45″ (1.5 kpc) to the west of the nucleus and has a velocity gradient consistent with material which lies within 1–2 kpc of the nucleus. Most of the asymmetry observed in the molecular emission is associated with this component, since no comparable emission is observed on the east side. The feature is also asymmetric in velocity, being redshifted at the nucleus with respect to the systemic velocity. Alternatively, one can consider this component to be centered at the systemic velocity, but offset 18″–25″ to the west of the nucleus. The ridge does not have the signature of expansion, but rather of an offset component undergoing rotation. It is also unlikely to represent a ring because there is no evidence for an intensity enhancement at either extremity. Other possibilities are a rotating molecular bar or an inner asymmetric spiral arm. Since there is abundant evidence for star formation throughout this component, we favor the spiral arm interpretation. The asymmetry/offset may be due to the tidal interaction with NGC 3627.

While the low velocity gradient component itself may not represent a bar, there is some reason to suspect that NGC 3628 may harbor a hidden bar. It is well known that bars are efficient catalysts for transporting gas from the surrounding interstellar medium into the nuclear regions of galaxies. A stellar bar typically sweeps gas down to a scale about one-tenth of its original size. On the smaller scale, another bar forms due to instabilities and the process can repeat (Friedli & Martinet 1993). Ishizuki (1995), in fact, has suggested an evolutionary sequence for barred galaxies in which a variety of CO morphologies result, depending on the stage of the starburst. For example, as gas is swept inward, an inner dense disk builds up (similar to that observed in NGC 3628), followed by the development of an outer gaseous ring in which star formation can also proceed. Also, given that this galaxy is known to be interacting with its companions, a bar or oval distortion is expected on dynamical grounds. There is, as yet, no evidence for a stellar bar in NGC 3628. However, the galaxy is edge-on, and a bar would be difficult to identify optically. Observations of NGC 3628 in the infrared may help to decide this matter (see Block & Wainscoat 1991).

4.4. *Expanding Bubbles, Extraplanar* CO *and Outflows*

One of the most interesting results of these observations is the discovery of expanding molecular shells (Table 2). All the identified shells occur within a few kpc of the nucleus, but outside the nuclear molecular disk itself. Since there is also evidence for star formation within the disk (§ 4.1), the absence of detectable shells in the nuclear disk may be a result of the higher ambient density in that region or because the starburst in this region is too young to produce detectable shells. Three of the observed shells center on the low velocity gradient ridge, while one (feature D) is offset in velocity from it. The emission in the shell rims is also very clumpy, possibly due to compression in shocks and/or instabilities.

The shells have energies of order 10^{52} to a few 10^{54} ergs ($\mathscr{X}\mathscr{D}^2$), requiring the input of 10–$1000\mathscr{X}\mathscr{D}^2$ supernovae. Oka et al. (1995) have recently observed an expanding molecular ring in the Galactic center of comparable energy (10^{54} ergs). It is interesting that all characteristic ages, τ (an upper limit to the "true" age), agree to within a factor of 2. This suggests that the shells formed at about the same time in a single burst of star formation within the last few $\times 10^6$ $\mathscr{D}$ years. Determining the characteristic expansion timescales is potentially an excellent way to "date" a starburst and could be very useful for testing starburst models. For example, fixing a time for onset of starbursting as a function of radius may help to constrain both inflowing bar-driven gas models (e.g., Ishizuki 1995) as well as outflowing disk-halo wind models. For this to be accomplished, a sufficient number of shells must be resolved.

There is clearly disk-halo outflow occurring in NGC 3628, observable in the X-ray emission, the radio continuum emission, the Hα emission, and now in the CO emission as well. The molecular outflows are implied through direct detection of CO out to 430 pc in projection from the midplane (see Fig. 4*a*), through the existence of expanding molecular shells, and through peculiarities in the velocity field, such as the northward opening velocity cone $\approx 20''$ to the west of the nucleus (Fig. 4*b*). The maximum z extent of the CO observed in NGC 3628 is larger than that observed in our own Galaxy (cf. 300 pc; T. Dame 1995). Detailed comparisons between the CO and outflow features observed at other wave bands is not straightforward, given the different spatial scales involved. However, there is one feature which correlates well. This is the Hα plume which extends over 4 kpc toward the south and intersects the disk at a position 20″ to the west of the nucleus (Fabbiano et al. 1990) This is exactly the position of shell D, at the apex of the northward opening velocity cone, as well as the most southerly CO extensions. Therefore, these features likely have a common origin and suggest that gas has broken out of the disk into the halo, with the net CO flow on the north side increasingly redshifted with distance from the plane (see isovelocity contours of Fig. 4*b*). It would be interesting to measure the velocity of the Hα plume on the south as a function of distance from the plane also, since this information may help to constrain the geometry of the event.

Note that the total CO line width depends not only on the rotation curve and line-of-sight distance sampled within the beam, but also on the superposition of the expanding features. With some shells spanning up to several hundred km s^{-1} in velocity, there are positions at which the total CO line width is actually dominated by collective expansion velocities of shells. This should be borne in mind when wide lines are observed from single-dish spectra. It has also been suggested (Rots 1978; Baan & Goss 1992) that the perturbed velocity field in the nuclear region of NGC 3628 is due to a tidal interaction with NGC 3627. This could be the case for the low velocity gradient ridge. However, at least some velocity perturbations (e.g., the cone) can be interpreted in terms of disk-halo outflow or other expansion velocities.

5. CONCLUSIONS

The main results of this paper are summarized below.

1. The molecular emission in the nucleus of NGC 3628 can be characterized by three main components: (*a*) a dense rotating nuclear molecular disk with a steep velocity gradient which dominates the emission, (*b*) a low velocity gradient ridge offset from the nucleus and likely within a few kpc of the nucleus, and (*c*) multiple expanding molecular shells.

2. The nuclear molecular disk is strongly centrally concentrated and is centered at the radio continuum peak which corresponds to the nucleus of the galaxy. Most of the detected molecular emission resides in this disk.

3. The nuclear molecular disk has been modeled successfully with an exponentially declining density distribution of radial scale length of $228\mathscr{D}$ pc and vertical scale height of $49\mathscr{D}$ pc, where $\mathscr{D}$ is the distance to the galaxy in units of 6.7 Mpc. The rotation curve can be characterized, to within the accuracy of the observations, by a Brandt curve with a peak velocity of 167 km s^{-1} at a radius of $61\mathscr{D}$ pc.

4. A velocity dispersion of 36–45 km s^{-1} is required to account for the line widths. The energy input from star-forming activity in the nuclear disk appears to be sufficient to account for this agitation.

5. The detected molecular mass constitutes from 18–33 $\mathscr{X}\mathscr{D}$% of the total dynamical mass within a central $230\mathscr{D}$ pc radius region, where $\mathscr{X}$ is the CO to H_2 conversion factor in units of 3×10^{20} cm^{-2} (K km $s^{-1})^{-1}$. The range reflects the uncertainty as to what fraction of gas in the region is bound.

6. The CO emission is very clumpy, both within and outside of the nuclear molecular disk. Clumps have masses in the range, 5×10^5–1.3×10^6 $\mathscr{X}\mathscr{D}$ $M_\odot$. Comparison of these masses with those expected for virialized clouds suggests that $\mathscr{X}$ may be lower than values observed in the Galactic disk.

7. The low velocity gradient ridge observed to the west of the nucleus is associated with star-forming activity and could represent an inner offset spiral arm. The asymmetry could result from the tidal interaction between NGC 3628 and one or more companions.

8. CO extensions/arcs can be seen out to $\approx 430\mathscr{D}$ pc from the midplane in projection.

9. Expanding molecular shells of kinetic energy 10^{52}–10^{54} $\mathscr{X}\mathscr{D}^2$ ergs are observed, most of which are associated with the low velocity gradient ridge. Characteristic timescales suggest that the starburst that produced these shells occurred within the last few 10^6 $\mathscr{D}$ years.

10. Expanding shell D, a northward opening velocity cone, and southern extensions are observed at a position 20″ to the west of the nucleus. This position corresponds to the apparent origin of the >4 kpc long Hα plume observed toward the south and suggests a common origin for these features.

Note added in manuscript.—Dahlem et al. (1996) report the discovery of an enormous X-ray halo around NGC 3628 with a total extent 40 kpc along the minor axis. Our estimate of mechanical energy input within the central 5″ radius region of the nuclear disk ($L \approx 3 \times 10^{41}$ ergs s^{-1}) is consistent with their range ($L \approx 2 \times 10^{41}$–$10^{42}$ ergs s^{-1}), which applies to the total central starburst, and has been estimated using different assumptions. Our results are also consistent with the suggestion that the origin of the X-ray halo is the central starburst, but we would place this origin just outside of the region containing the dense nuclear molecular disk, i.e., within approximately a kpc of the nucleus, rather than within the 230 pc radius disk. This does not preclude the possibility of future outflow through the nuclear disk, itself, when the current O star population become supernovae.

The authors wish to thank M. Dahlem for Hα and X-ray images of NGC 3628 in advance of publication. J. I. has been supported by the Natural Sciences and Engineering Research Council of Canada under grant WFA0156373.

REFERENCES

Anantharamaiah, K. R., Zhao, J.-H. Goss, W. M., & Viallefond, F. 1993, ApJ, 419, 585
Baan, W. A., & Goss, W. M. 1992, ApJ, 385, 188
Bally, J., Stark, A. A., Wilson, R. W., & Henkel, C. 1987, ApJS, 65, 13
Binney, J., & Tremaine, S. 1987, Galactic Dynamics (Princeton: Princeton Univ. Press)
Block, D. L., & Wainscoat, R. J. 1991, Nature, 353, 48
Boissé, P., Casoli, F., & Coombes, F. 1987, A&A, 173, 229
Braine, J., Combes, F., Casoli, F., Dupraz, C., Gérin, M., Klein, U., Wielebinski, R., & Brouillet, N. 1993, A&AS, 97, 887
Carlstrom, J. 1988, Ph.D. thesis, Univ. California, Berkeley
Carral, P., Turner, J. L., & Ho, P. T. P. 1990, ApJ, 362, 434
Condon, J. J. 1987, ApJS, 65, 485
———. 1992, ARA&A 30, 575
Condon, J. J., Condon, M. A., Gisler, G., & Puschell, J. J. 1982, ApJ, 252, 102
Condon, J. J., Helou, G., Sanders, D. B., & Soifer, B. J. 1990, ApJS, 73, 359
Dame, T. M. 1995, in IAU Symp. 170, CO: 25 Years of Millimeter-wave Spectroscopy, in press
de Vaucouleurs, G., de Vaucouleurs, A., Corwin, H. G., Jr., Buta, R. J., Paturel, G., & Fouqué, P. 1991, Third Reference Catalogue of Bright Galaxies (New York: Springer-Verlag) (RC3)
Downes, D., Radford, S. J. E., Guilloteau, S., Guélin, M., Greve, A., & Morris, D. 1992, A&A, 262, 424
Downes, D., Solomon, P. M., & Radford, S. J. E. 1993, ApJ, 414, L13
Dressel, L. L., & Condon, J. J. 1976, ApJS, 31, 187
Dumke, M., Krause, M., Wielebinski, R., & Klein, U. 1995, preprint
Fabbiano, G. 1988, ApJ, 330, 672
Fabbiano, G., Heckman, T., & Keel, W. C. 1990, ApJ, 355, 442
Friedli, D., & Martinet, L. 1993, A&A, 277, 27
Garcia, A. M. 1993, A&AS, 100, 47
Haynes, M. H., Giovanelli, R., & Chincarini, G. L. 1984, ARA&A, 22, 445
Haynes, M. H., Giovanelli, R., & Roberts, M. S. 1979, ApJ, 229, 83
Irwin, J. A. 1994, ApJ, 429, 618
Irwin, J. A., & Seaquist, E. R. 1988, ApJ, 335, 658
———. 1991, ApJ, 371, 111; erratum 415, 415
Ishizuki, S. 1995, in IAU Symp. 170, CO: 25 Years of Millimeter-wave Spectroscopy, in press

Ishizuki, S., Kawabe, R., Ishiguro, M., Okumura, S. K., Morita, K.-I., Chikada, Y., & Kasuga, T. 1990, Nature, 344, 224
Israel, F. P., Baas, F., & Maloney, P. R. 1990, A&A, 237, 17
Kenney, J. D. P., Carlstrom, J. E., & Young, J. S. 1993, ApJ, 418, 687
Kenney, J. D. P., Wilson, C. D., Scoville, N. Z., Devereux, N. A., & Young, J. S. 1992, ApJ, 395, L79
Lequeux, J. 1983, A&A, 125, 394
MacLaren, I., Richardson, K. M., & Wolfendale, A. W. 1988, ApJ, 333, 821
Morris, M. 1995, in IAU Symp. 170, CO: 25 Years of Millimeter-wave Spectroscopy, in press
Nakai, N., Hayashi, M., Handa, T., Sofue, Y., Hasagawa, T., & Sasaki, M. 1987, PASJ, 39, 685
Nilson, P. 1973, Uppsala General Catalogue of Galaxies (Uppsala Astron. Obs. Ann., 6)
Oka, T., Hasegawa, T., Handa, T., Sato, F., & Tsuboi, M. 1995, in IAU Symp. 170, CO: 25 Years of Millimeter-wave Spectroscopy, in press
Reuter, H.-P., Krause, M., Wielebinski, R., & Lesch, H. 1991, A&A, 248, 12
Rice, W., Lonsdale, C., Soifer, B., Neugebauer, G., Kopan, E., Lloyd, L., de Jong, T., & Habing, H. 1988, ApJS, 68, 91
Rickard, L. J., Bania, T. M., & Turner, B. E. 1982, ApJ, 252, 147
Rickard, L. J., & Harvey, P. M. 1984, AJ, 89, 1520
Rickard, L. J., Turner, B. E., & Palmer, P. 1985, AJ, 90, 1175
Roberts, M. S. 1975, in Galaxies and the Universe, ed. A. Sandage, M. Sandage, & J. Bristian (Chicago: Univ. Chicago Press), 309
Rots, A. H. 1978, AJ, 83, 219
Rubio, M. 1995, in IAU Symp. 170 (abstracts), CO: 25 Years of Millimeter-wave Spectroscopy, 25
Schlickeiser, R., Werner, W., & Wielebinski, R. 1984, A&A, 140, 277
Schmelz, J. T., Baan, W. A., & Haschick, A. D. 1987a, ApJ, 315, 492
———. 1987b, ApJ, 320, 145
Seaquist, E. R., Davis, L. E., & Bignell, R. C. 1978, A&A, 63, 199
Sodroski, T., et al. 1995, ApJ, submitted
Sofue, Y. 1995, in IAU Symp. 170 (abstracts), CO: 25 Years of Millimeter-wave Spectroscopy, 27
Tifft, W. G., & Cocke, W. J. 1988, ApJS, 67, 1
Turner, J. 1994, in Mass-Transfer Induced Activity in Galaxies, ed. I. Shlosman (Cambridge: Cambridge Univ. Press), 90
van der Hulst, J. M., Crane, P. C., & Keel, W. C. 1981, A&A, 86, 1175
van Gorkom, J. H., & Ekers, R. D. 1986, in Synthesis Imaging, ed. R. A. Perley, F. R. Schwab, & A. H. Bridle (Green Bank: National Radio Astronomy Observatory), 177
Wilding, T., Alexander, P., & Green, D. A. 1993, MNRAS, 263, 1075
Wray, J. D. 1988, The colour Atlas of Galaxies (New York: Cambridge Univ. Press)
Young, J. S., & Scoville, N. Z. 1991, ARA&A, 29, 581
Young, J. S., Tacconi, L. J., & Scoville, N. Z. 1983, ApJ, 269, 136